Effect of Doping in Defective Half-Heusler $Nb_{0.8}CoSb$

A Thesis

submitted to

Indian Institute of Science Education and Research Pune in partial fulfillment of the requirements for the BS-MS Dual Degree Programme

by

Lalith Kumar Gurram

Indian Institute of Science Education and Research Pune

Dr. Homi Bhabha Road,

Pashan, Pune 411008, INDIA.

April, 2023

Supervisor: Dr. Surjeet Singh

1. Certificate

This is to certify that this dissertation entitled "Effect of Doping on the $Nb_{0.8}CoSb$ Defective Half-Heusler" towards the partial fulfillment of the BS-MS dual degree program at the Indian Institute of Science Education and Research, Pune represents study/work carried out by Lalith Kumar Gurram at Indian Institute of Science Education and Research under the supervision of Name of Dr. Surjeet Singh, Professor, Department of Physics, during the academic year 2022-2023.

Dr. Surjeet Singh

Committee:

Dr. Surjeet Singh

Dr. Prasenjit Ghosh

Declaration

I hereby declare that the matter embodied in the report entitled "Effect of Doping on the $Nb_{0.8}CoSb$ Defective Half-Heusler" Here are the results of the work carried out by me at the Department of Physics, Indian Institute of Science Education and Research, Pune, under the supervision of Dr. Surjeet Singh, and the same has not been submitted elsewhere for any other degree.

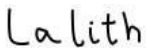

Lalith Kumar Gurram

Table of Contents

List of Figures

List of Tables

Abstract

A thermoelectric (TE) device converts heat energy into electrical energy and can be used to tap the waste heat and turn it into clean and useful electrical energy that can reduce our dependence on fossil fuels whose excess use has led to climate change and global warming. The efficiency of a TE device depends on the figure of merit (zT) of the n-type and p-type materials used in its fabrication. The higher the zT, the greater the efficiency. The zT of the TE material is given by the formula: $zT = S^2\sigma/k$ where S is the Seebeck coefficient, σ is the electrical conductivity and k is the thermal conductivity at an absolute temperature T. Some of the most commonly used TE materials include PbTe, Bi_2Te_3, etc. They exhibit a reasonably high zT (>1) near room-temperature; however, their applicability in the mid-to-high temperature range is severely limited by their low-melting temperatures.

In this regard, the alloys of the Heusler family, and half-Heusler (hH) XYZ with valence electron could (VEC) 18 as they are stable in particular, have attracted a great deal of attention. They have high melting temperatures and their closed-shell electronic structure ensures good semiconducting properties but the main disadvantage of it is they have high thermal conductivity. The NbCoSb system, despite having a 19-valence electron count (VEC), stabilizes itself in $Nb_{0.8}CoSb$ by introducing vacancies at the Nb site. These vacancies contribute to a reduction in thermal conductivity, resulting in a maximum thermoelectric figure of merit (zT) of 0.9 at 1123K in $Nb_{0.83}CoSb$.

In my work, I attempted to substitute Si and Al at the Sb site, but the Al doping was incomplete and the enhancement in Si doping was less than the highest reported value. Additionally, I attempted to achieve resonant doping in $Nb_{0.8}CoSb$ using Mo and W doping at the Nb site, but resonant doping did not occur. However, there was an enhancement in transport properties, and a zT of 0.88 was achieved at approximately 973K with 0.5% Mo doping. The cause of this enhancement is still being investigated.

Acknowledgments

I am deeply grateful to my thesis supervisor, Dr. Surjeet Singh, for his unwavering support and guidance throughout my research journey. His constructive feedback helped me correct my mistakes in experimental work, and his ideas provided valuable solutions when I was stuck. His mentorship allowed me the freedom to explore new avenues, which helped me to grow as a researcher.

I am grateful to my Ph.D. mentor, Ankit Kumar, for his invaluable support. He taught me essential experimental techniques and shared his knowledge, which significantly contributed to the success of my research. I would like to extend my thanks to Navita for her insightful discussions and Sagar for accompanying me in trekking and various activities. I am grateful for my labmates, Luminata Ma'am, Dibyata, Navita, Ankit, Nashra, Sagar, Dinesh, Rupesh, Pankaj, Arindam, and Vishak, for their wonderful company in the lab and during chai breaks, and for waiting for me till I finished my lunch.

I would like to express my gratitude to my batchmates for their continuous support and for bearing with me despite my imperfect Hindi, and to my childhood friends for making difficult times bearable during the COVID lockdown. I would also like to extend special thanks to Great Indian Treks (GIT) for providing opportunities to experience the breathtaking beauty of Maharashtra through trekking.

I would like to express my gratitude to Mr. Anil, Mr. Sudheer, Mr. Nilesh Dumre, and all the staff members at H-cross for their valuable contributions towards the completion of my work. I am also thankful to the Infosys Foundation for awarding me a scholarship during my BSMS.

Finally, I would like to thank my Maa for always believing in me, and my family for their unwavering support.

Chapter-1

Introduction

The primary energy sources currently in use are fossil fuels, nuclear and renewable energy. These energy sources have limitations and dangers such as finite resources, environmental impact, nuclear waste, and dependence on weather conditions. Most energy generated from these sources is wasted and sent back to the environment as waste heat. Fig 1.1 explains the energy utilization from different sources.

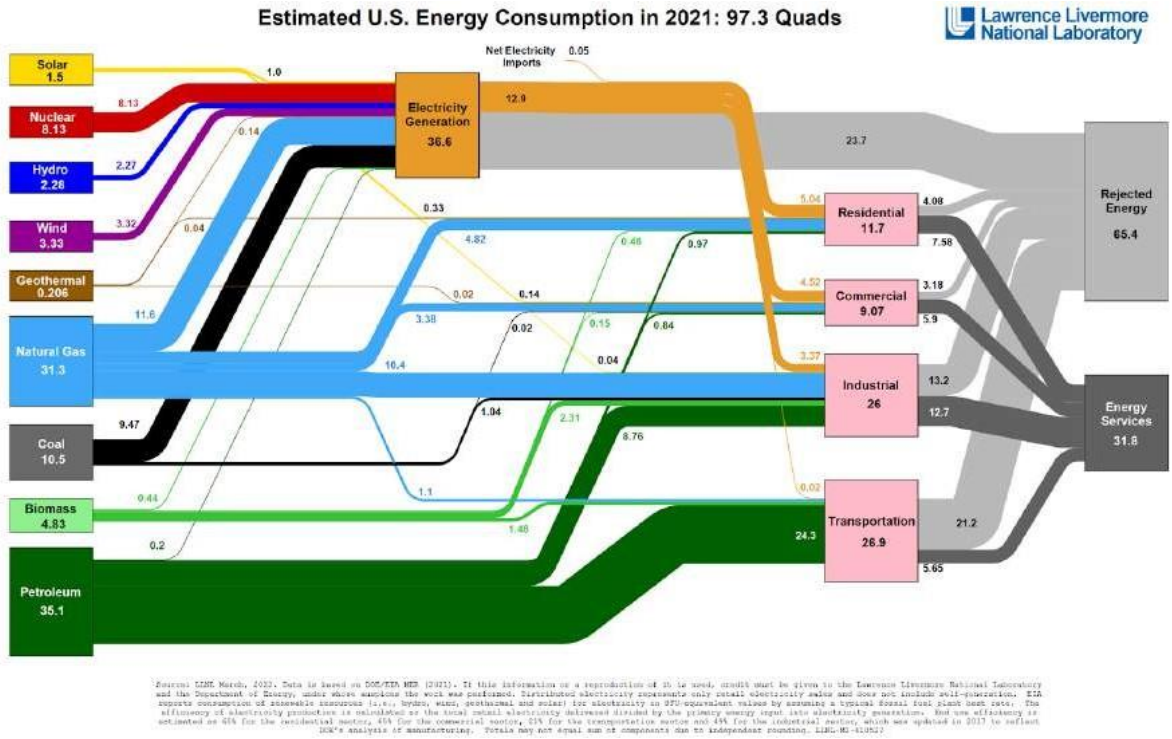

Fig 1.1: Energy consumption of the US in 2021[1]

There is a strong need to develop renewable energy sources to reduce energy wastage and decrease greenhouse gas emissions and air pollution. Additionally, it can decrease dependence on finite resources, reduce the risk of nuclear accidents and the potential for nuclear weapons proliferation, and minimize the environmental impact of hydroelectric projects. While there may not be a single perfect solution, the utilization of thermoelectrics can play a significant role in addressing these challenges as thermoelectrics can convert waste heat into electrical energy and can use electrical energy to create heating and cooling effects.

Thermoelectric generators have the ability to improve the efficiency of a heat source when installed. They are currently used in satellites for power generation and in the automobile industry [2]. The advantages of thermoelectrics include no moving parts, no greenhouse gas emissions, and silent operation, but they also have limitations such as low conversion efficiencies, high costs, and high densities [3]. The goal is to find thermoelectric materials that have high efficiency at relatively lower costs.

1.1 Thermoelectricity

Thermoelectricity is the phenomenon in which heat and electric charge are closely linked. When a temperature gradient is applied to thermoelectric devices, electricity is generated. Conversely, a temperature gradient is generated when a potential gradient is applied. The phenomenon of thermoelectricity is caused by three main effects: the Seebeck effect, the Peltier effect and the Thompson effect.

Seebeck Effect: When a temperature difference is applied across an electrically conducting material as shown in Fig 1.2, a potential difference is generated across the ends of the material. The potential difference formed under a steady state is given by the formulae, $\nabla V = -S\nabla T$ Where S is the Seebeck coefficient. The Seebeck is positive for p-type materials and negative for n-type materials. The principle behind the working of a thermocouple is the Seebeck effect.

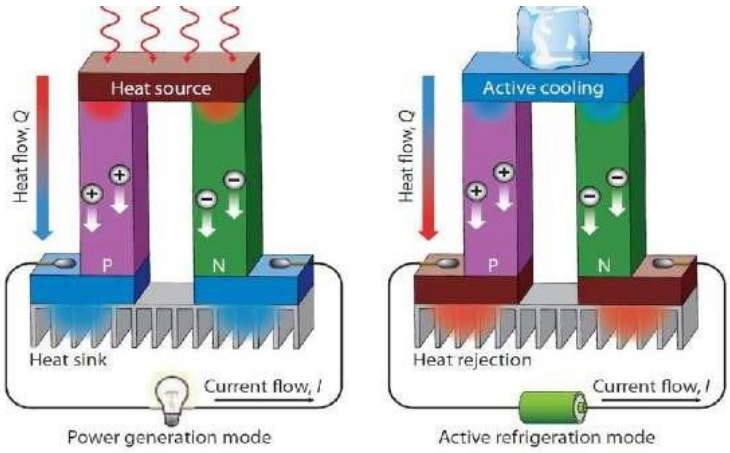

Fig 1.2: Seebeck and Peltier effects respectively(taken from[4])

Peltier Effect: The Peltier effect is opposite to the Seebeck effect. Here we pass current through the electrically conducting material as shown in Fig1.2; it will generate a temperature difference across its ends. The heat generated per unit time is given by the formulae. $\dot{Q} = \Pi T$ Where Π is the Peltier coefficient. Since Seebeck and Peltier effects are related, their coefficients are also connected by the relation $\Pi = TS$. Solid-state heat pumps work by the principle of the Peltier effect.

Thompson Effect: When a current is passed through a conductor with a temperature gradient, different Peltier cycles occur throughout the conductor, resulting in local heating and cooling.

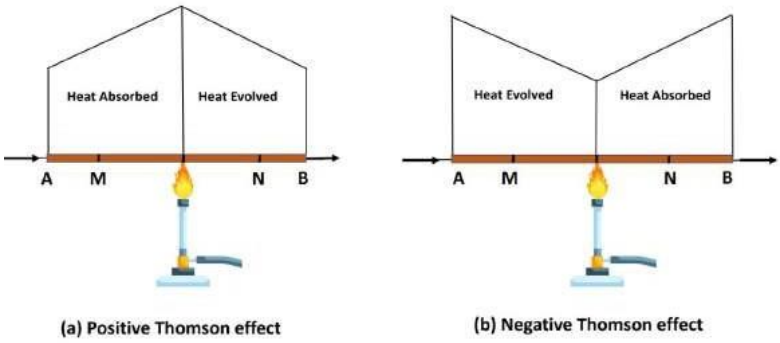

Fig 1.3: Positive and Negative Thomson effect.

As indicated in Fig 1.3, there are two types of Thomson effects: positive and negative. In the positive Thomson effect, the starting end of the conductor gets cooled, while in the negative Thomson effect, it is heated. This variation is not due to the p and n-type nature of the material alone. A p-type material can show either positive or negative Thomson effects, or it can show both positive and negative effects at different temperatures. The nature of the material could depend on factors like temperature, carrier concentration, and band structure. Thomson effects must be considered for practical applications. Even in thermocouples, Thomson corrections are included.

1.2 Thermoelectric devices

A thermoelectric device typically consists of both P-type and N-type thermoelectric legs as shown in Fig 1.4, which are electrically connected in series and thermally connected in parallel, with ceramic plates covering both ends of the legs.

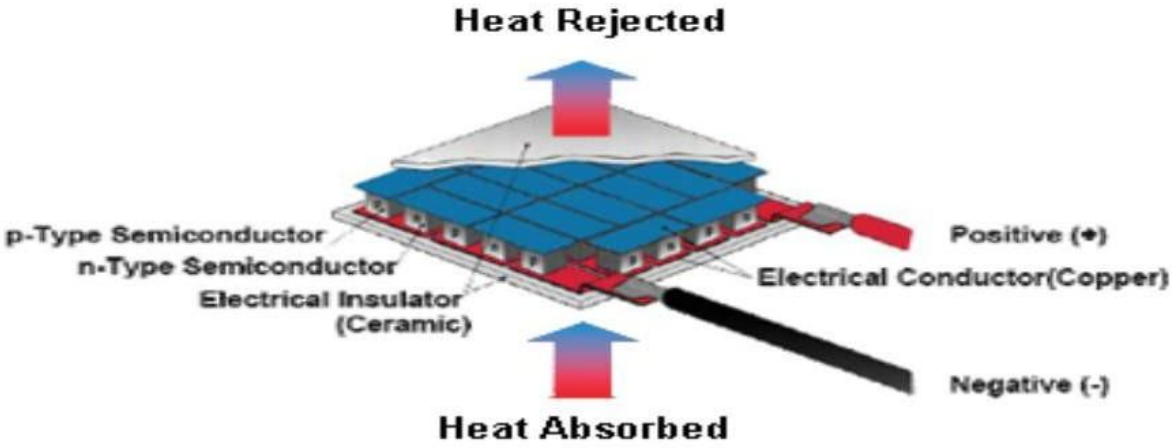

Fig 1.4: Thermoelectric module[5]

While a device with only one type of leg is possible, a two-leg device is more practical. When used as a thermoelectric cooler, the Coefficient of Performance (COP) is defined as the heat extracted from the source divided by the electrical energy expended. If there are no losses due to electrical resistance or heat conduction, the COP value should be equal to that of a Carnot cycle. The COP of the Carnot cycle is given by $T_h/T_h - T_c$, where T_h is the temperature of the hotter side and T_c is the temperature of the cooler side. For a real thermoelectric cooler, the optimum COP(ϕ_{max}) is given by

$$COP = \frac{\gamma T_c - T_h}{\Delta T(\gamma + 1)} \quad \text{where} \quad \gamma = \sqrt{1 + Z(\frac{T_c + T_h}{2})} \quad [6]$$

Z is the Figure Of Merit (FOM) of the device and is defined by

$$Z = \frac{(S_p - S_n)^2}{[(\kappa_p \rho_p)^{\frac{1}{2}} + (\kappa_n \rho_n)^{\frac{1}{2}}]^2}$$

S_p and S_n are the Seebeck coefficients of the P and N-type legs. Similarly κ refers to thermal conductivity and ρ refers to electrical resistivity.

Similarly, for a thermoelectric generator, the optimum efficiency is given by the relation

$$\eta = \frac{\Delta T(\gamma - 1)}{\gamma T_h + T_c} \quad [6]$$

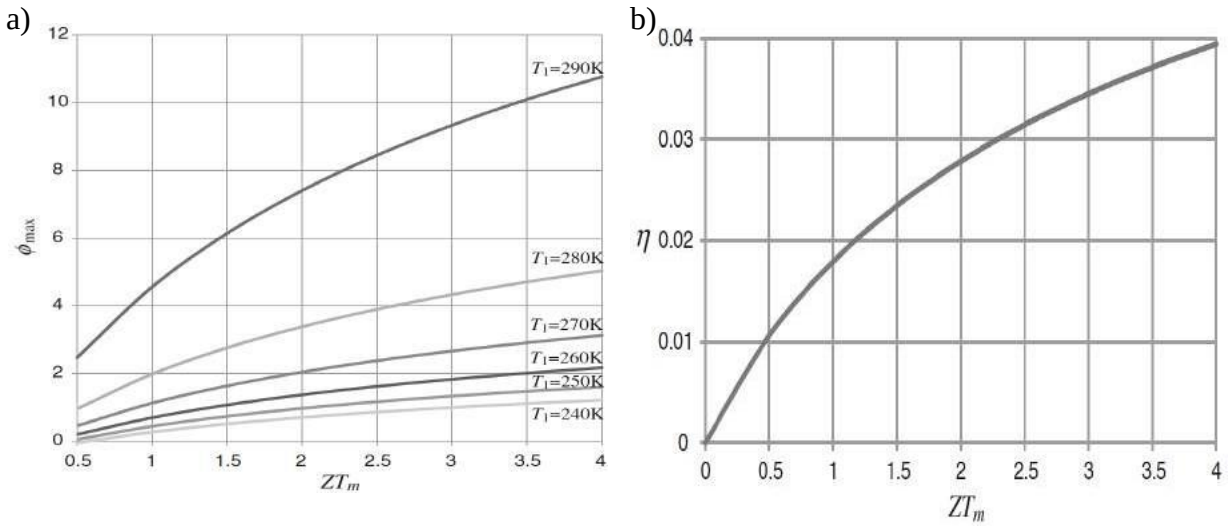

Fig 1.5: a) Dependence of $\Phi_{max}$with ZT [6]and b) Dependence of η with ZT [6]

Fig 1.5 clearly indicate that the higher the ZT value, the greater the efficiency. Hence, the primary objective of thermoelectric research is to enhance the figure of merit.

1.3 Transport Coefficients

ZT represents the device's figure of merit, while zT represents the material figure of merit defined by $zT = S^2\sigma T/\kappa$. To achieve a high ZT, a material with a high zT should be selected. The goal is to synthesize and optimize materials to achieve a high zT. To increase zT, the transport properties must be optimized. However, optimizing the transport properties is not an easy task as they are interdependent. To understand these coefficients deeply, the Landauer-Boltzmann approach is needed, but for now, we will try to understand them using the Single Parabolic Band (SPB) model.

According to the SPB model, the Seebeck coefficient is defined by

$$S = \frac{8\pi^2 k_B^2}{3eh^2} m^* T \left(\frac{\pi}{3n}\right)^{\frac{2}{3}} \quad [7]$$

$$m^* = N_V^{\frac{2}{3}} \times m_b^*$$

$$\mu \propto \left(\frac{1}{m_b^*}\right)^{\frac{5}{2}} \quad [7]$$

m^* is the Density Of States (DOS) effective mass, which represents the average over many electronic bands. m_b^* is the band effective mass of a particular band defined as

$$m_b^* = \frac{\hbar^2}{d^2E/d^2k}$$

n is the carrier concentration, μ is the mobility, N_V is the valley degeneracy and T is the temperature.

As per the above relations, increasing the carrier concentration results in a decrease in the Seebeck coefficient and an increase in the electrical conductivity. On the other hand, increasing the DOS effective mass leads to an increase in the Seebeck coefficient but a decrease in the electrical conductivity due to reduced mobility. Thermal conductivity (κ) is composed of two parts: electrical (κ_e) and lattice (κ_l). The component κ_l is independent of carrier concentration, but the κ_e depends on carrier concentration through electrical conductivity according to the

Wiedemann-Franz law, $\kappa_e = \sigma LT$, where L is Lorentz's number that can be calculated by the formulae

$$L = 1.5 + e^{\left[\frac{-|S|}{116}\right]}$$ [8]

Therefore, an optimal carrier concentration is required to achieve a peak zT. The Pisarenko plot in Fig 1.6 clearly illustrates these relationships.

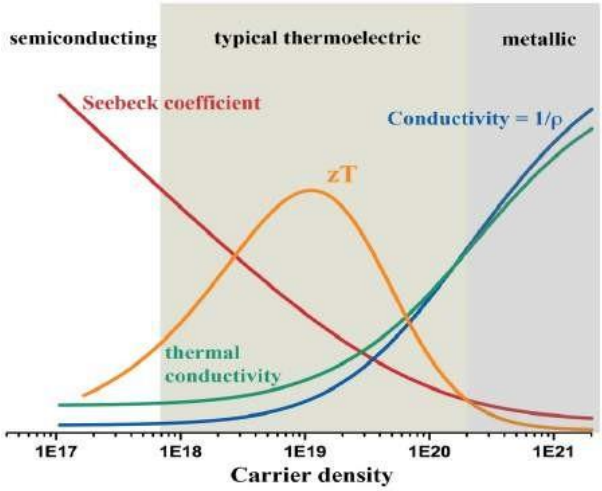

Fig 1.6: Pisarenko plot[9]

1.4 Ways to improve zT

There are two main strategies that can be employed to improve the dimensionless figure of merit (zT) of a material. The first strategy involves improving the power factor and the second involves reducing thermal conductivity. Let us see how this can be done.

1.4.1 Power Factor Enhancement

Carrier optimization:

We saw earlier that electrical conductivity and the Seebeck coefficient are inversely related, and the power factor reaches a maximum value at a specific carrier concentration. Therefore, tuning carrier concentration is the best way to improve the power factor, and it can be achieved by

doping with a suitable element. Carrier doping is similar to p and n-type doping in Si and Ge semiconductors[10].

Band Convergence:

When electronic bands start to converge, such as through doping or a change in composition, the band effective (m_b^*) mass increases. When bands align, the valley degeneracy (N_V) increases. These effects can increase the DOS effective mass (m^*), increasing the Seebeck coefficient. For a single parabolic Band Model, the relation is given by

$$S = \frac{8\pi^2 K_B^2}{3eh^2} m^* T \left(\frac{\pi}{3n}\right)^{\frac{2}{3}} \quad \text{Where} \quad m^* = N_V^{\frac{2}{3}} \times m_b^*$$

This strategy has been used in the material $Mg_2Si_{1-x}Sn_x$, where the convergence occurred due to changes in the composition of Sn (x)[11].

Modulation doping:

In this approach, nano inclusions are added to the bulk material. These inclusions donate carriers to the bulk but remain otherwise disconnected from them. As a result, materials are free from ionized impurity scattering encountered in the conventional doping. This improves carrier mobility and hence increases the electrical conductivity[12]. Moreover, these nano inclusions also reduce thermal conductivity, further improving the value. zT

The modulation doping technique has been used in GaAs-$Al_xGa_{1-x}As$ superlattice structures to enhance the mobilities[13].

Resonant Doping:

Here, by doping around 1% of impurity atoms, the density of states (DOS) near the Fermi level gets distorted due to the contribution of electronic states of the impurity atom. This leads to an increase in the Seebeck coefficient, as Mott's theory states that is directly proportional to the slope of the density of states at the Fermi energy (EF). The enhanced Seebeck coefficient leads to an increase in the power factor. Formation of Resonant states is illustrated in Fig 1.7

In section 3.4, we will see examples of resonant doping and how to select the resonant dopant in Half- Heuslers.

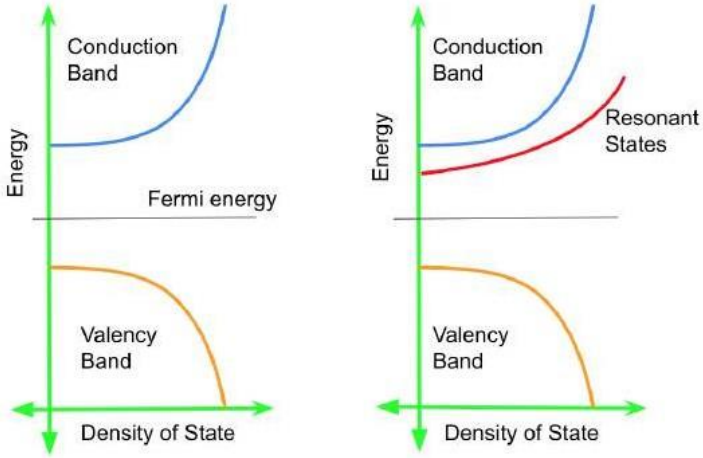

Fig 1.7: Formation of resonant states

Energy Filtering:

Energy filtering is an efficient tool for a material with high carrier concentration. In this effect, the low-energy carriers are blocked by barriers, making them inaccessible for transport. This reduces the effective carrier concentration but increases mobility, maintaining the electrical conductivity and leading to an increase in the Seebeck coefficient. These barriers could be grain boundaries or other dopants. Dopants should be chosen so that their Fermi energy level is greater than the Fermi energy of the bulk.

The nanocomposites of PbTe demonstrate an enhancement in the seebeck coefficient when compared to single crystal and polycrystalline PbTe due to the energy filtering created by the grain boundaries[14].

1.4.2 Thermal Conductivity Reduction

Nanostructuring:

Creating nanostructured materials can be an effective way to reduce thermal conductivity. This is achieved by restricting the phonons with higher mean free path, making them unavailable for

heat transport. In addition, grain boundary scattering increases in nanostructured materials, further reducing thermal conductivity.

Upon nanostructuring, there is a reduction in the thermal conductivity of a p-type half-heusler which enhances the zT[15].

Alloying or dopant engineering:

Another approach is to introduce alloying elements into the material with different masses. The addition of alloying elements can introduce point defects and create lattice distortions, which scatter phonons and reduce the thermal conductivity.

The enhancement in zT of TiCoSb is observed through Ta doping and Hf alloying, which results in a reduction in thermal conductivity[16].

Fig 1.8 shows various scattering mechanisms present in nanostructured and alloyed materials.

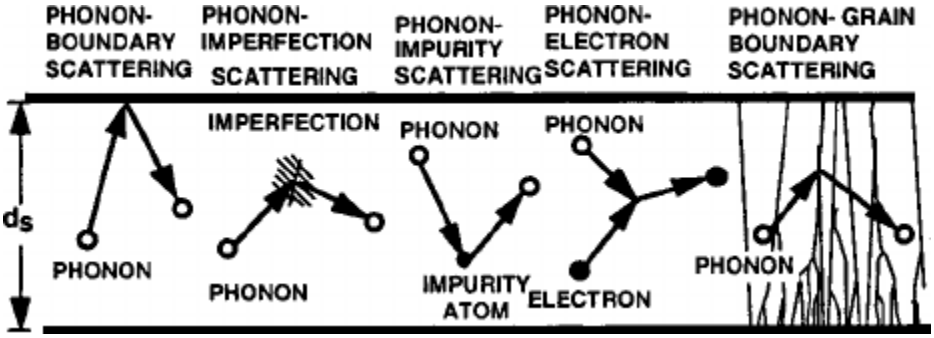

Fig 1.8: Phonon Scattering Mechanisms[17]

1.5 Half-Heulser

The general formula for Half-Heusler compounds is XYZ, where X and Y are distinct electropositive elements and Z is the most electronegative element. X and Y are typically d-block elements and Z is a P-block element. The crystal structure of these compounds belongs to space group no. 216, $F\bar{4}3m$, characterized by three interpenetrating FCC lattices[18].

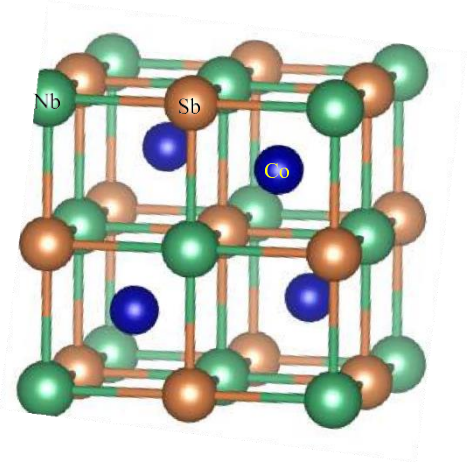

Fig 1.9: Half-Heusler NbCoSb

The bonding nature in half-Heusler compounds is a combination of ionic and covalent. The electronegative atoms Y and Z form a covalently bonded anionic network $[YZ]^{n-}$ in which the S and P orbitals of both Y and Z atoms participate in hybridization. The $[YZ]^{n-}$ and X^{n+} have a strong ionic interaction. Additionally, d orbitals of $[YZ]^{n-}$ and X^{n+} are involved in hybridization, forming bonding and antibonding orbitals, which create a gap. This gap in these compounds makes them promising materials for thermoelectric applications[19].

In the bonding process of half-Heusler compounds, the d orbitals of Y and the S and P orbitals of Z attempt to fill themselves with electrons from X. To fill them completely, a total of 18 valence electrons are needed from all these elements. Experimentally and theoretically, it has been observed that half-Heuslers with 18 valence electrons are more stable.

Half-Heusler compounds have several advantages, including high thermal stability, good mechanical strength, and relatively low cost. The main disadvantage of these compounds is their high thermal conductivity. They are also used in spintronics and other applications.

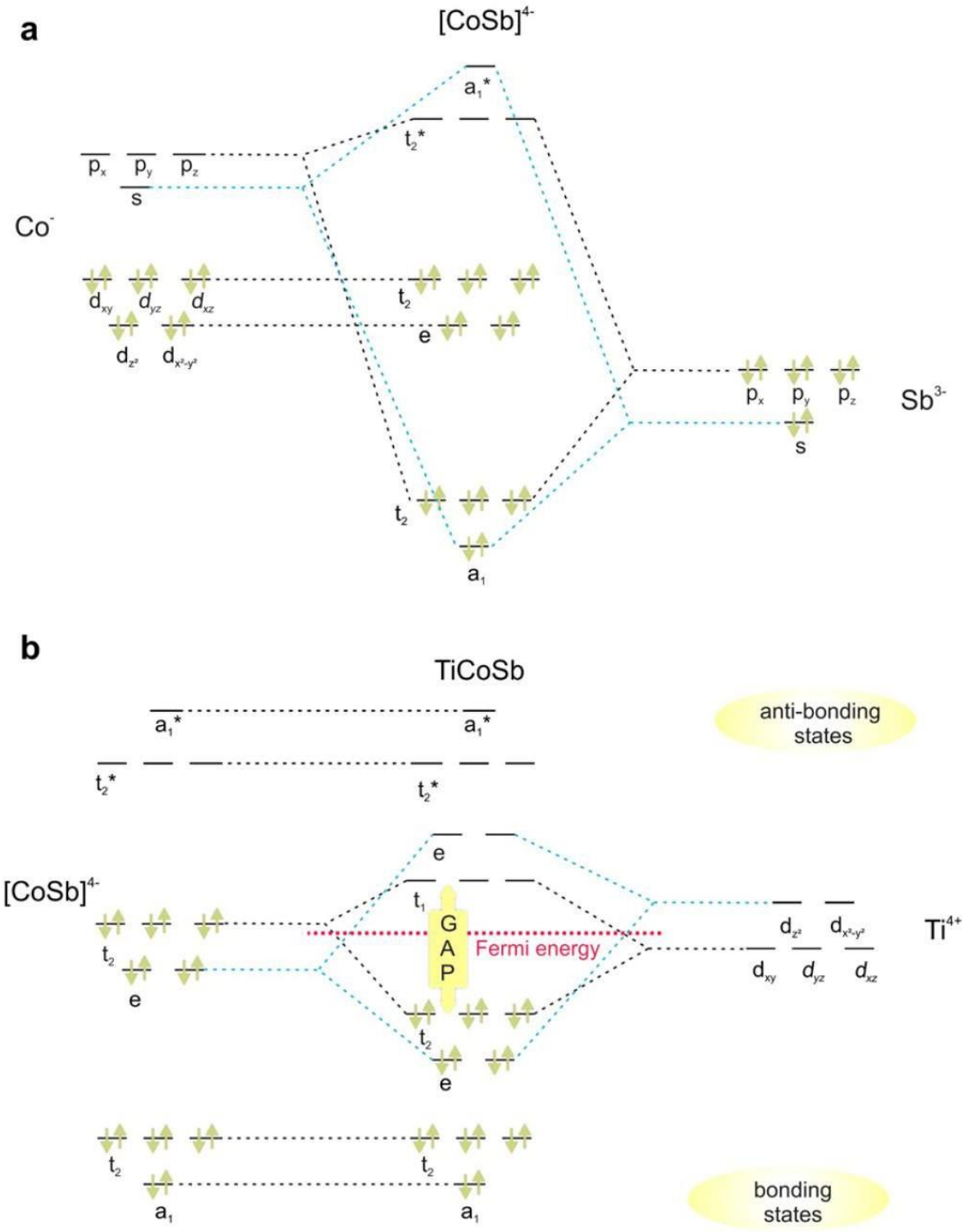

Fig 1.10: Molecular orbitals of TiCoSb[19]

1.5.1 NbCoSb

NbCoSb is a half-heusler with 19 valence electrons per formula unit. Although half-heuslers typically don't form with this number of valence electrons, NbCoSb forms with vacancies at the Nb site, resulting in 18 valence electrons per formula unit. Its pure form is $Nb_{0.8}CoSb$. The advantage of these vacancies is that they reduce the lattice thermal conductivity of phonons by scattering, but they also scatter electrons, resulting in a decrease in electrical conductivity and power factor. In the NbCoSb system, the electrical conductivity is sensitive to the Nb concentration. Xia et al. studied the effect of Nb stoichiometry on NbCoSb and found that the maximum zT value of 0.9 was achieved at 1123 K in $Nb_{0.83}CoSb$ [20].

In an attempt to build on previous work, Kumar Sourabh studied the effect of Sn doping at the Sb site in NbCoSb, and in his thesis, he demonstrated an increase in electrical conductivity with Sn doping. This can be attributed to the difference in electron contribution between Sb (5 e-) and Sn (4 e-), where replacing Sb with Sn results in a deviation from 18 VEC. To attain 18 VEC, the system incorporates more Nb, and since electrical conductivity is sensitive to the Nb site occupancy, an increase in Nb leads to an increase in electrical conductivity. Kumar Sourabh also collaborated with Dr. Prasenjit Ghosh's group for band structure calculations and found that at an Nb stoichiometry of 0.9, the bands near the conduction band minima (CBM) converge, enhancing the transport properties. Further, a new flat band appears near CBM within a few k_BT_R (T_R: room temperature) of the fermi energy, which prevents the Seebeck coefficient from decreasing with Nb doping [21].

As part of my MS, I have studied the effects of other dopants like Si, Al, Ga, In, and Ge in my work and have tried to achieve Nb0.9 stoichiometry by altering the Nb and Sb sites. I have also tried resonant doping in NbCoSb with Mo and W at the Nb site.

Chapter-2

Experimental Techniques

2.1 Synthesis

2.1.1 Arc melting

Arc melting is a method of synthesizing materials by melting their constituent elements in the right proportions. The proportions are calculated based on the formula unit with a Molecular Lentech Calculator; later, I developed a code in Python. The process starts by loading the weighted elements into the chamber, followed by purging with argon gas to remove any oxygen. A high potential is established between the tungsten tip and copper base (the base is cooled continually by water supply while melting), creating an arc by quickly touching and removing the tip. Before melting the elements, a zirconium getter is melted to absorb residual oxygen. The melted ingot is flipped and remelted multiple times, usually 3-4 times, to achieve homogeneity.

a)

b)

c)

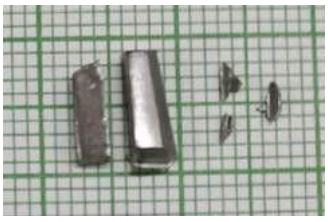

Fig 2.1: a) Arc Melting furnace b) Cobalt and Antimony c) Available Nb in two different sizes.

On the left side of the Fig 2.1(c) are long bars of Nb and on the right are tiny pieces cut from an Nb rod. There are a few difficulties while melting, like, the difference in melting points of the elements being too large. Nb has a melting point of 2469^{o}C and Sb has melting and boiling points of 630.6^{o}C and 1635^{o}C respectively. Thus, even before Nb starts melting, Sb starts boiling making it difficult to get a homogeneous melt. My seniors have optimized the synthesis technique in which we take 10% extra Sb by weight to compensate for the loss. By comparing the weights before and after melting, we can estimate how much Sb is present in the sample.

In our lab, we had two different forms of raw Nb, as shown in the figure. Depending on availability, we chose different Nb for different sample synthesis. Further details are provided in Chapter 3.

2.1.2 Sintering

The ingot formed through arc melting is hand-grinded for one hour using an agate mortar and pestle. The resulting powder is loaded into an 8mm die set and cold pressed by applying a 3-ton load using a KBr press. The pellets are then carefully placed inside preheated quartz tubes and connected to a vacuum pump. After creating a vacuum of 10^{-3} torr, the quartz tubes are sealed and placed inside a furnace at 1100^{o}C for 7 days. On the final day, the tubes are removed with care and quickly quenched in an ice bath.

Fig 2.2: pellets ceiled in vacuum[21]

We have used this process for the 1 set of samples. Later on, we used Hot Press.

2.1.3 Hot Press

Hot Pressing is a technique in which the pellets are pressed at higher temperatures and high pressures in a vacuum. We have used graphite die sets. These die sets are covered inside with graphite sheets before use so that the pellets don't stick to the die sets. The heating is done by the coil placed inside the chamber through the process of Induction heating. We have a pyrometer attached outside the vacuum chamber which senses the IR radiation spectrum of the graphite die and measures the temperature of the system. If the temperature of the die set is not equal to the set temperature, the pyrometer passes a signal to the power source to increase the current in the coil.

a) b)

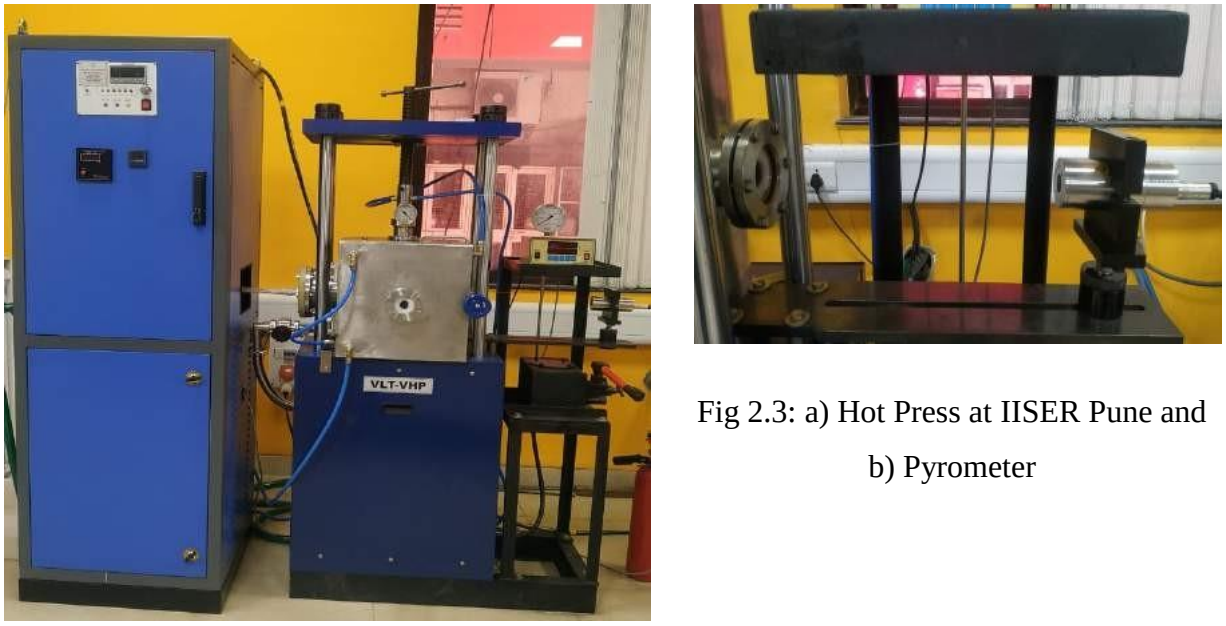

Fig 2.3: a) Hot Press at IISER Pune and b) Pyrometer

The first set of samples is hot-pressed at 1050°C, and subsequent samples are pressed at 1010°C under a force of 4.5KN using a 8mm die set for 10 minutes. After pressing, the graphite layer is removed by polishing it with sandpaper, followed by 360-grit polishing paper.

2.2 Structural Characterization

2.2.1 X-ray Diffraction (XRD)

X-ray Diffraction is a useful tool for checking the purity of crystalline materials. Atoms in crystalline materials are arranged periodically. When electromagnetic waves with wavelengths comparable to interatomic distances of the material are incident on the sample, the waves diffract. X-rays, whose wavelength is comparable to the interatomic distances of the crystal, are used to study the crystal. Constructive interference results in a peak in intensity at specific angles given by Bragg's law :

$$2\ d \sin\theta = n\ \lambda$$

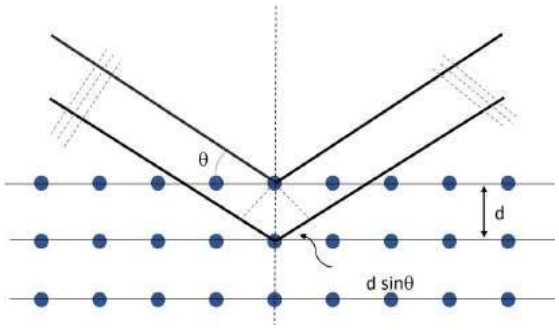

Fig 2.4: diffraction of X-rays from a periodic lattice.

where d is the interatomic distance, θ is the angle of incidence, λ is the wavelength of the incident x-ray, and n is a natural number. We used the powder XRD technique to check the purity of the samples, which involves grinding the sample into a fine powder and placing it on a glass slide with sticky oil. The slide is loaded into a sample holder and placed in the lab-based Bruker D8 Advance diffractometer at IISER Pune.

The X-rays used for the analysis are generated by the Cu target, while the K_β reflections are blocked by the Ni filter placed in the detector. To eliminate $K\alpha_2$ and the background, EVA software is used. For the analysis, $K\alpha_1$ with a wavelength of 1.5406 $\mathring{A}$ is used. The EVA software has an XRD database using which we check the purity of the sample. The XRD data is plotted using the Origin software, with 2θ as the x-axis and intensity as the y-axis. To determine the lattice parameters, Reitveld refinement is performed using Full-Prof software. In this

technique, the experimentally measured data is fit with a theoretical model by adjusting various parameters until the best match is obtained. The refinement is repeated several times, changing some parameters defined in the software to obtain the closest values of lattice parameters.

a) b)

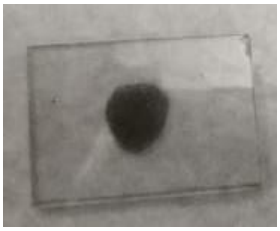

Fig 2.5: a) XRD slide and b) Bruker D8 Advance Diffractometer at IISER Pune.

2.2.2 Field Emission Scanning Electron Microscopy (FESEM)

FESEM is a technique that is used to analyze the sample's surface morphology, elemental composition and measure the dimensions of nanostructures. It has a Field Emission gun that uses a high electric field to extract electrons from a sharp tip of the metal and produces a highly collimated electron beam, which can be focused to a small size. The working of an SEM is similar to that of an optical microscope, with the difference being that x-rays replace the light rays and magnetic coils replace the lens. The SEM has multiple detectors for detecting different emissions and reflections when the high-energy beam of electrons hit the sample, primary electrons are produced that are detected by the ASB detector, providing information about the sample's phases. The primary electrons also knock out electrons from the atoms' inner shell, resulting in secondary electrons that are detected by the SE2 and Inlens detectors, which are used to study the sample's morphology. The higher energy electrons also produce characteristic x-rays

as the electrons in higher energy states jump to lower energy states. The characteristic X-rays are detected and converted into electrical signals to form an Energy Dispersive X-ray Spectrom (EDS) that helps identify the elements present in the sample. However, detecting lighter elements like C and O is difficult because they emit low-energy X-rays that are challenging to detect.

a)

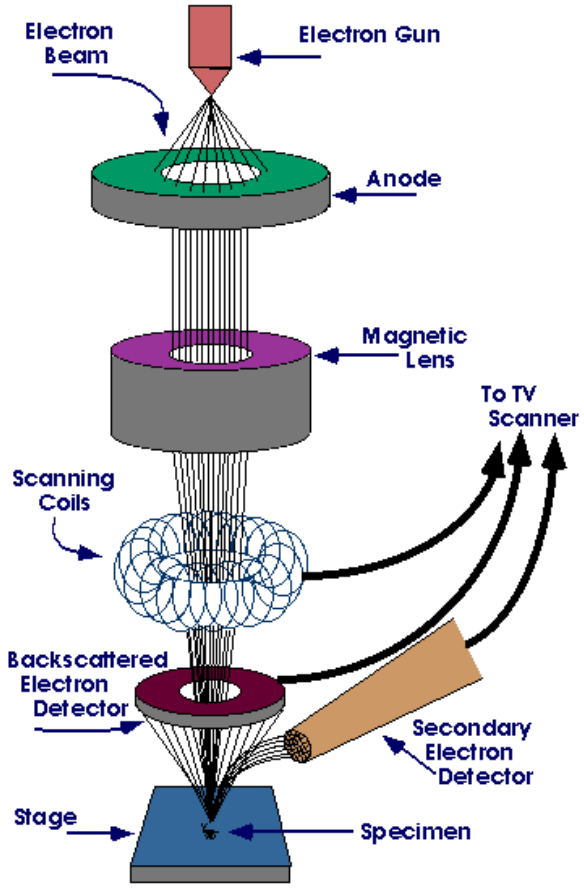

b)

Fig 2.6:a) Schematics of working of a FESEM[22] and b) FESEM at IISER Pune

2.3 Density Measurement

2.3.1 Archimedes Method

The densities of the samples whose shape is not regular are measured by the Archimedes method, using the formulae $\rho_s = \rho_l \left(\frac{m_a}{m_a - m_l} \right)$ where ρ_s and ρ_l are the densities of the

a) b)

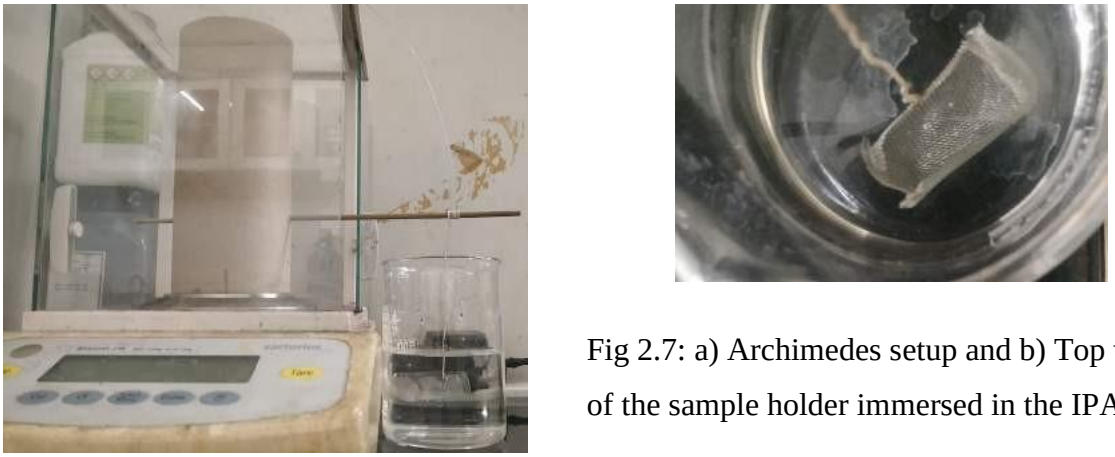

Fig 2.7: a) Archimedes setup and b) Top view of the sample holder immersed in the IPA

sample and the liquid, m_a and m_l are the masses of the sample in air and in liquid respectively. The mass in the air is directly measured using the weighing machine. The mass in liquid is measured by using the setup as shown in the image

The liquid we used is Isopropyl alcohol (IPA) which has a density of 0.786 g/cc at room temperature. With this setup, I have measured the density of Cobalt (Co) to be 8.76 g/cc, which is slightly lower than the true density of Co of 8.9 g/cc. Although the accuracy of the measurement was limited due to errors such as the evaporation of IPA, it provides a rough estimate of the density.

The hot-pressed samples were very dense and could be easily formed into regular shapes such as cuboids and cylinders. To determine their densities, we measured the mass (m) and volume (V) of the samples and used the formula $\rho = m/V$ to get the sample density.

2.4 Transport Properties Measurements

2.4.1 Linseis LSR-3

The Linseis LSR is used to measure electrical resistivity and the Seebeck coefficient, which can be measured from room temperature up to 1000°C. The system uses Halogen lamps for heating and is equipped with a feedback mechanism to maintain the desired temperature. However, it is important to consider factors such as sample oxidation, sample reaction with the probes, and deposition of the sample on the probes before performing measurements at high temperatures. Measurements for HH samples are performed up to 700°C and are conducted in a helium atmosphere. In order to reduce the effects of deposition, probes are polished with 1000 grit size polishing paper before loading the samples. A standard Constantan sample is also run routinely to make sure that the probes are working fine. If the Constantan run doesn't match the standard data, then the thermocouples are cut, and new junctions are made by welding them.

a) b)

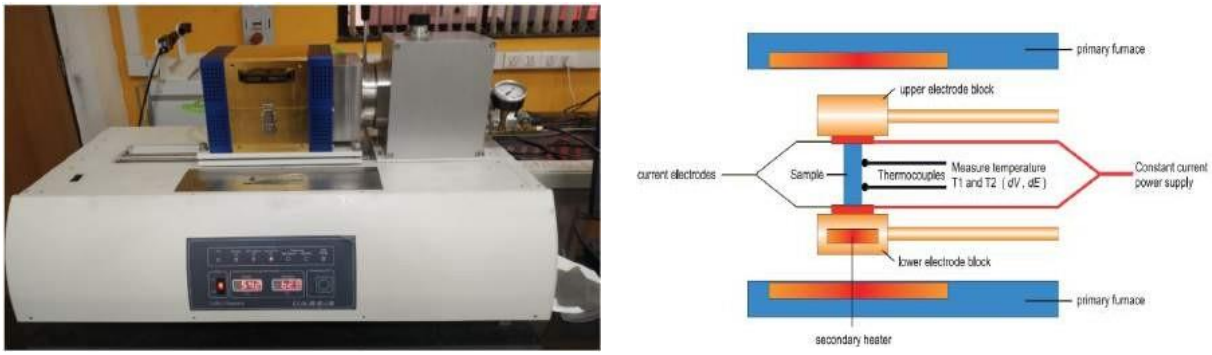

Fig 2.8: a) Linseis LSR 3 IISER Pune and b) schematic scheme of the inside of the LSR chamber taken from the LSR manual.

The electrical resistivity is measured using the four-probe method, as shown in the figure. A constant current of 20mA is passed through the sample using the upper and lower platinum probes, and the voltage drop is measured by the s-type thermocouples on the sides. The resistance is calculated using Ohm's law, and the resistivity is determined from the sample

dimensions. All the contacts are pressure contacts. To measure the Seebeck coefficient, a heater is installed in the lower electrode block to maintain a temperature gradient of 40K. The s-type thermocouples measure the temperature difference and the voltage drop at the contacts. The Seebeck coefficient is determined by the formula S = -dV/dT, which provides the relative Seebeck coefficient, considering that the probe Seebeck coefficient also contributes. The absolute Seebeck coefficient is calculated using the Ta.exe software.

Since a temperature gradient exists, the sample temperature is calculated as the average of the values measured by the thermocouples. Additionally, the measurements are taken within a temperature tolerance of 10K as it is not feasible to stabilize the temperature precisely at the required value.

2.4.2 Laser Flash Analysis(LFA)

LFA is used to measure the thermal diffusivity of the samples. The thermal conductivity is then calculated from the relation $\kappa(T) = \alpha(T)c_p\rho$, where κ is the thermal conductivity, α is the thermal diffusivity, ρ is the density and c_p is the specific heat capacity of the sample. The measurements are performed in a vacuum by keeping the vacuum pump always on during the measurement, and the pressure inside the chamber can reach up to 1.1 * 10^{-2} mbar. Prior to creating a vacuum, the chamber is purged several times with He gas. The measurements for HH
samples are performed up to 800°C, but the LFA can measure even higher temperatures, exceeding 1000°C.

The measurement begins with a laser pulse being flashed at the bottom side of the sample, causing it to heat up. The heat is then diffused through the sample, increasing the temperature of the top side. An IR detector is used to measure the time it takes for the top surface to heat up. The diffusivity is then measured by the formulae

$$\alpha = \frac{0.13879 \times l^2}{t_{0.5}}$$

Where l is the sample's thickness and $t_{0.5}$ is half-time for the top-side temperature to reach the maximum value. The above formula assumes the ideal situation, so LFA uses some mathematical models to extract the thermal diffusivity of the sample.

While performing LFA, certain preparations should be made before the measurement. For example, the sample should be coated with a graphite layer to ensure the laser pulse is completely absorbed by the sample. Additionally, the detector chamber should be filled with liquid nitrogen in order to keep the CCD in working temperature range.

a)

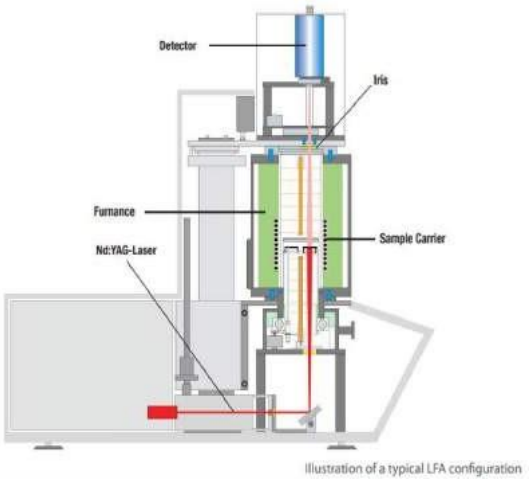

b)

c)

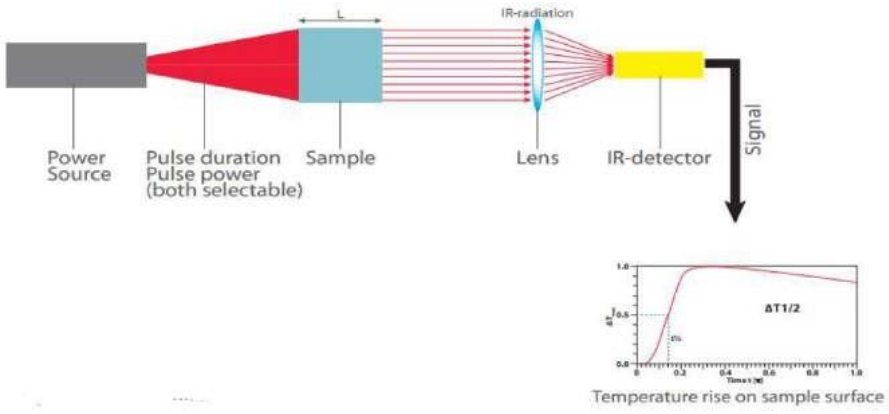

Fig 2.9: a) Schematics of LFA setup b) LFA at IISER pune and c) LFA measurement principle. The images are taken from LFA manual.

Chapter-3

Results and Discussion

In this chapter, I will present the work done in my MS thesis. In section 3.1, I will show the results of exploring the effect of Sb site doping in NbCoSb with various dopants. Section 3.2 will discuss the effects of high Al and Si doping at the Sb site. Section 3.3 will provide a detailed explanation of the Si series. In section 3.4, I will discuss the effects of W and Mo doping at the Nb site. Finally, in section 3.5, I will explore the effects of Mo doping in more detail.

3.1 Exploration of Sb site in $Nb_{0.8}CoSb$

I have tried doping Al, Si, Ga, Ge, In and Sn each with 5% doping at the Sb site. The stoichiometries are designed by keeping in mind the 18 VEC rule. The aimed stoichiometries are listed in Table 3.1. These samples are synthesized in arc melting followed by 1 hour of grinding and sintering at 1100^{o}C. In these samples, Nb bars are used as the source of Nb. The 6 samples are synthesized in two sets, in the first set extra 8% Sb is taken. Realizing that it won't be sufficient, in the next round 10% extra Sb is taken.

Sr No.	Sample	Extra Sb taken (by weight)	Sample Weight expected after arc melting (gm)	Sample Weight after arc melting (gm)
1	$Nb_{0.82}CoSb_{0.95}Al_{0.05}$	8%	1.5290	1.4742
2	$Nb_{0.81}CoSb_{0.95}Si_{0.05}$	8%	1.1087	1.0438
3	$Nb_{0.81}CoSb_{0.95}Sn_{0.05}$	8%	0.9779	0.9675
4	$Nb_{0.82}CoSb_{0.95}Ga_{0.05}$	10%	1.0841	1.0742
5	$Nb_{0.82}CoSb_{0.95}In_{0.05}$	10%	0.9512	0.9480
6	$Nb_{0.81}CoSb_{0.95}Ge_{0.05}$	10%	1.0598	1.0176

Table 3.1: Nominal composition with extra Sb taken, expected and obtained weight of the samples.

The VEC is determined by adding up the electron contributions from each element, based on the number of valence electrons in their outermost shell. For instance, Nb contributes 5 valence electrons, Co contributes 9 valence electrons, Sb contributes 5 valence electrons, and so on. By summing up the valence electron contributions from all elements in the formula unit, the VEC is found to be 18.

3.1.1 XRD

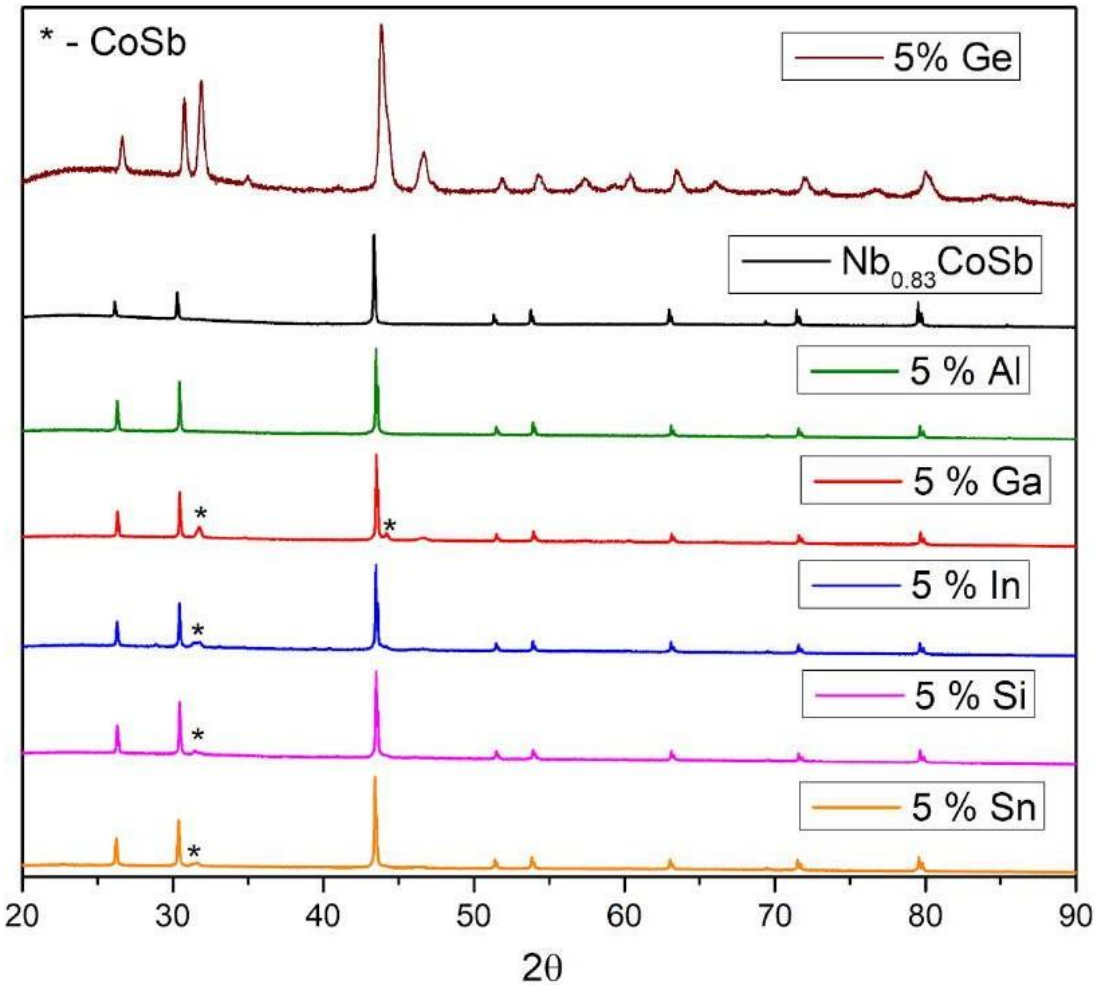

Fig 3.1: XRD pattern of Al, Si, Ge, Ga, In and Sn doping at the Sb site of $Nb_{0.8}CoSb$

The peaks indicated by the star symbol representing the CoSb phase. The black curve shows $Nb_{0.83}CoSb$ from my semester project's work, used for comparison with the results obtained from a standard half-Heusler phase.

Based on the powder XRD data, it can be concluded that except for Ge, the main phase in all other dopants is the Half-Heusler phase. Al, on the other hand, shows no detectable parasitic phases, which indicates that it has formed a pure phase. For the rest of the dopants, the parasitic CoSb phase is present in small amounts. Additionally, small amounts of unidentified impurity phases are found in the case of In and Ga doping. However, due to their low percentages, it was difficult to identify them through XRD. Thus, it can be inferred that Ge doping would not be effective, whereas other dopants work and with further improvement in the synthesis method, they may all form nearly 100% pure HH phase.

When the samples were hand-grinded, it was found that the Nb did not melt homogeneously due to its high melting point and the larger size of the Nb pieces taken during melting. Through XRD analysis, the presence of unreacted Nb was confirmed. The Nb-rich pieces were physicality separated and the resulting powder was then cold pressed and sintered at 1100^{o}C for 7 days. XRD analysis of the sintered samples is shown below.

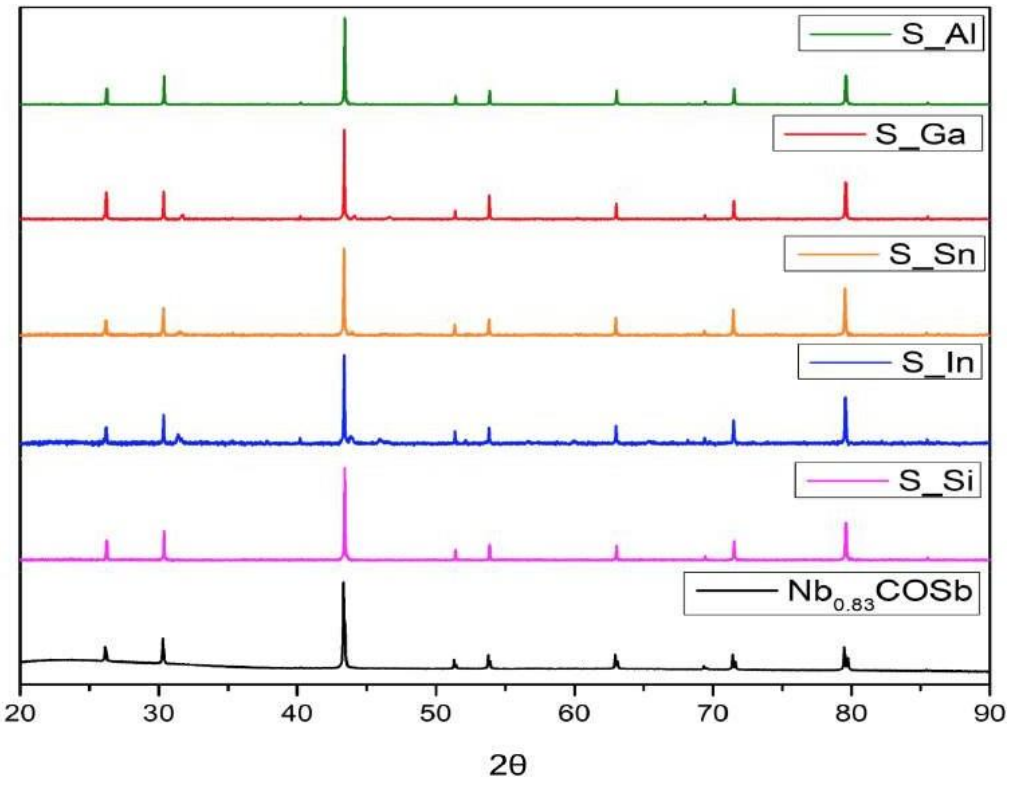

Fig 3.2: Sintered XRD pattern of Al, Si, Ge, Ga, In and Sn doping at the Sb site of $Nb_{0.8}CoSb$

While the majority phase in all the cases is HH, the impurity phases remained and in some cases increased even further. Only the Si doped sample appears to remain single phase. On the other hand, the Al doped sample, which was nearly a single phase after arc-melting has shown the presence of small extra peaks after sintering for 7 days.

3.1.2 Transport Properties

a)

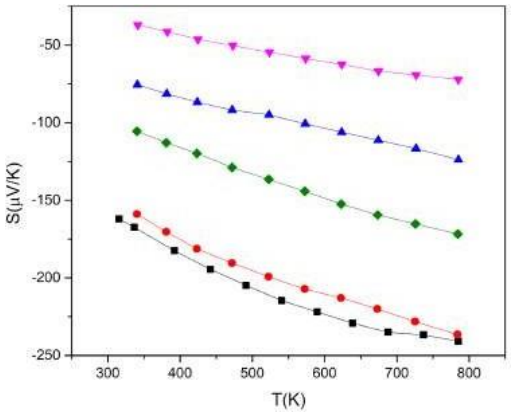

b)

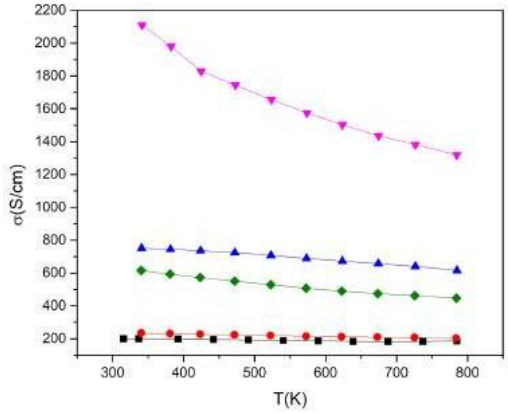

c)

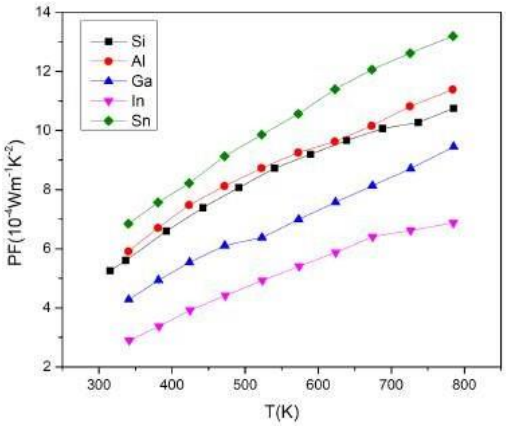

Fig 3.3: Seebeck coefficient, Electrical conductivity, and Power factors of Al, Si, Ge, Ga, In and Sn doping at the Sb site of $Nb_{0.8}CoSb$

Before analyzing the data let's recollect that $\sigma \propto n$ and $S \propto n^{\frac{-2}{3}}$. The electrical conductivities and Seebeck coefficients for these dopings exhibit a particular trend. This trend suggests that the carrier concentration is the primary factor that changes with doping. However, it should be noted that the presence of unmelted Nb and other phases in some samples may also affect the transport properties. Nevertheless, studying the preliminary samples can help us determine the appropriate dopants for further investigation.

Based on the XRD and LSR data, we can eliminate Ge, Ga, and In doped samples, and focus on Si and Al for further study. These dopings resulted in pure samples in the detectable range of XRD and demonstrated high Seebeck values which are essential for a good thermoelectric material. However, the electrical conductivities were low, potentially due to a lower concentration of Nb.

3.2 Achieving $Nb_{0.9}$ stoichiometry by doping

As we have learned in section 1.6 that at an Nb stoichiometry of 0.9, the NbCoSb HH exhibits better transport properties according to the theory. In my work, I have tried to achieve Nb0.9 by doping with Al and Si. Since the HH is stable at 18 VEC, I have designed the stoichiometries in such a way the total VEC is maintained at 18. I prepared samples with increasing Al or Si doping, and accordingly, I increased the Nb stoichiometry to maintain VEC 18. The sample's stoichiometry is given in Table 3.2. For example, take $Nb_{0.86}CoSb_{0.85}Al_{0.15}$, the VEC is 5 0.86 + 9 + 5 0.85 + 3 0.15 = 18. Since we had unmelted Nb in the trial samples, I decided to cut the Nb bar into smaller pieces in order to allow Nb to melt homogeneously. For these samples, I have taken 10 % extra Sb to compensate for the losses during melting.

The lattice parameters are calculated using the Rietveld Refinement. The lattice parameters are listed in Table 3.2. A decrease in the lattice parameters is observed, which proves that the Si and Al are incorporated into the structure. When compared to $Nb_{0.83}CoSb$, the lattice parameters of these samples are expected to be less because Al and Si have a smaller ionic radius than Sb. The Al-doped sample has a smaller lattice parameter than Si because Al is smaller than Si.

Sr No.	Sample	Lattice parameters(A^o)
1	$Nb_{0.83}CoSb$	5.900316
2	$Nb_{0.82}CoSb_{0.9}Si_{0.1}$	5.897748
3	$Nb_{0.83}CoSb_{0.85}Si_{0.15}$	5.899933
4	$Nb_{0.84}CoSb_{0.9}Al_{0.1}$	5.895044
5	$Nb_{0.86}CoSb_{0.85}Al_{0.15}$	5.895521

Table 3.2: Chemical formulae and the lattice parameters of 10% and 15% of Al and Si at the Sb site of $Nb_{0.8}CoSb$

3.2.1 XRD

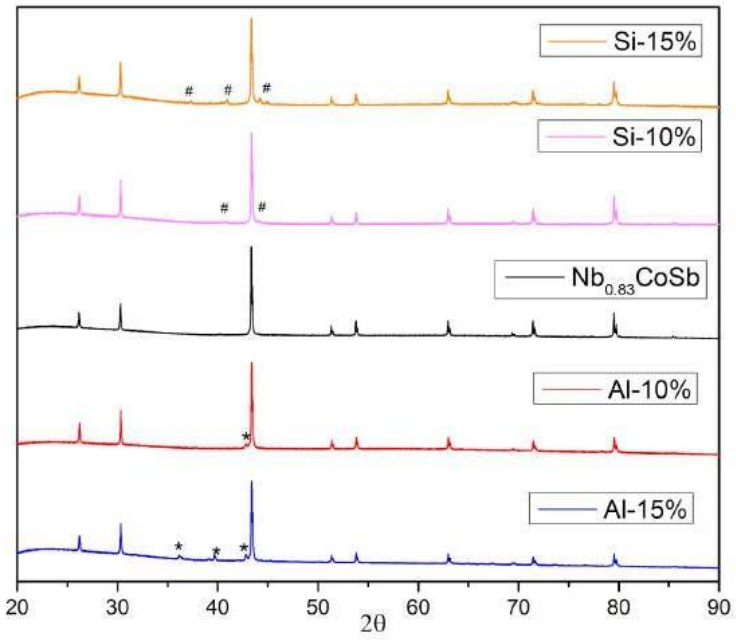

Fig 3.4: XRD of 10% and 15% of Al and Si at the Sb site of $Nb_{0.8}CoSb$

The XRD data show that the higher doping of Si and Al samples are not forming the pure phase. From 10 to 15% doping the impurities increased. Which means the solubility of Si and Al is less. The impurity phase in Si-doped samples is identified as Co_3Nb_2Si, but for the Al-doped samples,

there was no match in the database. As of now, it is still an unknown phase. Although band calculations show a good feature at $Nb_{0.9}$ stoichiometry, it is not possible to stabilize $Nb_{0.9}$ stoichiometry with Al and Si doping. Therefore it leaves us to explore the low doping of Si and Al.

3.3 Exploring lower doping of Si

I synthesized three Si-doped samples with doping percentages of 1%, 2.5%, and 5% while maintaining a stoichiometry of 18 valence electron counts (VEC). The chemical formulas for each sample are listed in Table 3.3. To overcome the problem of incomplete melting of Nb, a different synthesis technique was employed. Initially, Nb and Co were melted together, followed by melting this NbCo ingot with the other precursors, namely Sb and Si. This technique was used as Nb and Co have higher boiling points, allowing for longer melting time. Consequently, Nb completely melted and formed NbCo, which has a melting point between Nb and Co, enabling easy melting with the other precursors.

After arc melting these samples are hand grinded, cold pressed and sintered at 1100^{o}C for 7 days.

3.3.1 XRD

The XRD shows that all three samples are in a pure phase. The lattice parameters are shown in Table 3.3.

Sr No	Sample	Lattice Parameter(A^{o})
1	$Nb_{0.83}CoSb$	5.9003
2	$Nb_{0.802}CoSb_{0.99}Si_{0.01}$	5.8960
3	$Nb_{0.805}CoSb_{0.975}Si_{0.025}$	5.8946
4	$Nb_{0.81}CoSb_{0.95}Si_{0.05}$	5.8961

Table 3.3: Chemical formulae and lattice parameters of 1%, 2.5% and 5% Si doping at the Sb site of $Nb_{0.8}CoSb$

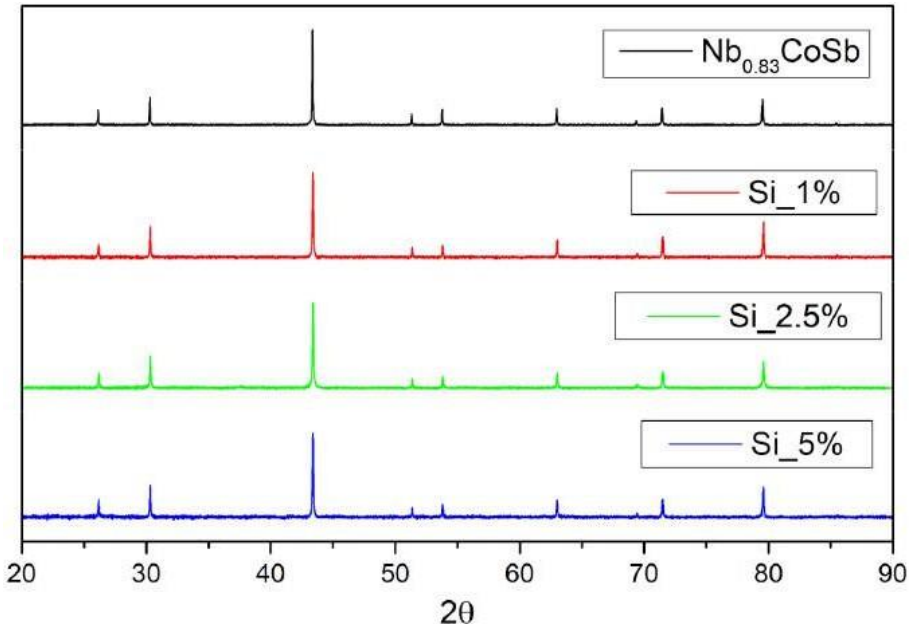

Fig 3.5: XRD pattern of 1%, 2.5% and 5% Si doping at the Sb site of $Nb_{0.8}CoSb$

The smaller size of Si compared to Sb results in a decrease in lattice parameter with increasing Si doping. This decrease is observed in the lattice parameter for the Si-doped samples, indicating that Si is entering the lattice. However, it is observed that there is no further decrease in the lattice parameter beyond a doping level of 2.5%. This could be due to the fact that increasing the Nb composition results in an increase in the lattice parameter.

3.3.2 FESEM

The FESEM data of the sintered samples revealed that they are not completely in the pure phase. The impurity phase Co_3Nb_2Si was identified in the SEM image of all three samples. Although XRD was unable to detect this due to its small quantity. This was detected due to its different contrast in the SEM images, and upon EDS and chemical mapping, the composition Co : Nb : Si ☰ 3 : 2 : 1 was revealed. Additionally, we also observed some contrast but the EDS composition still revealed Nb : Co : Sb : Si composition similar to the main HH phase. It is likely that this contrast is due to the different crystallographic orientation of the grain.

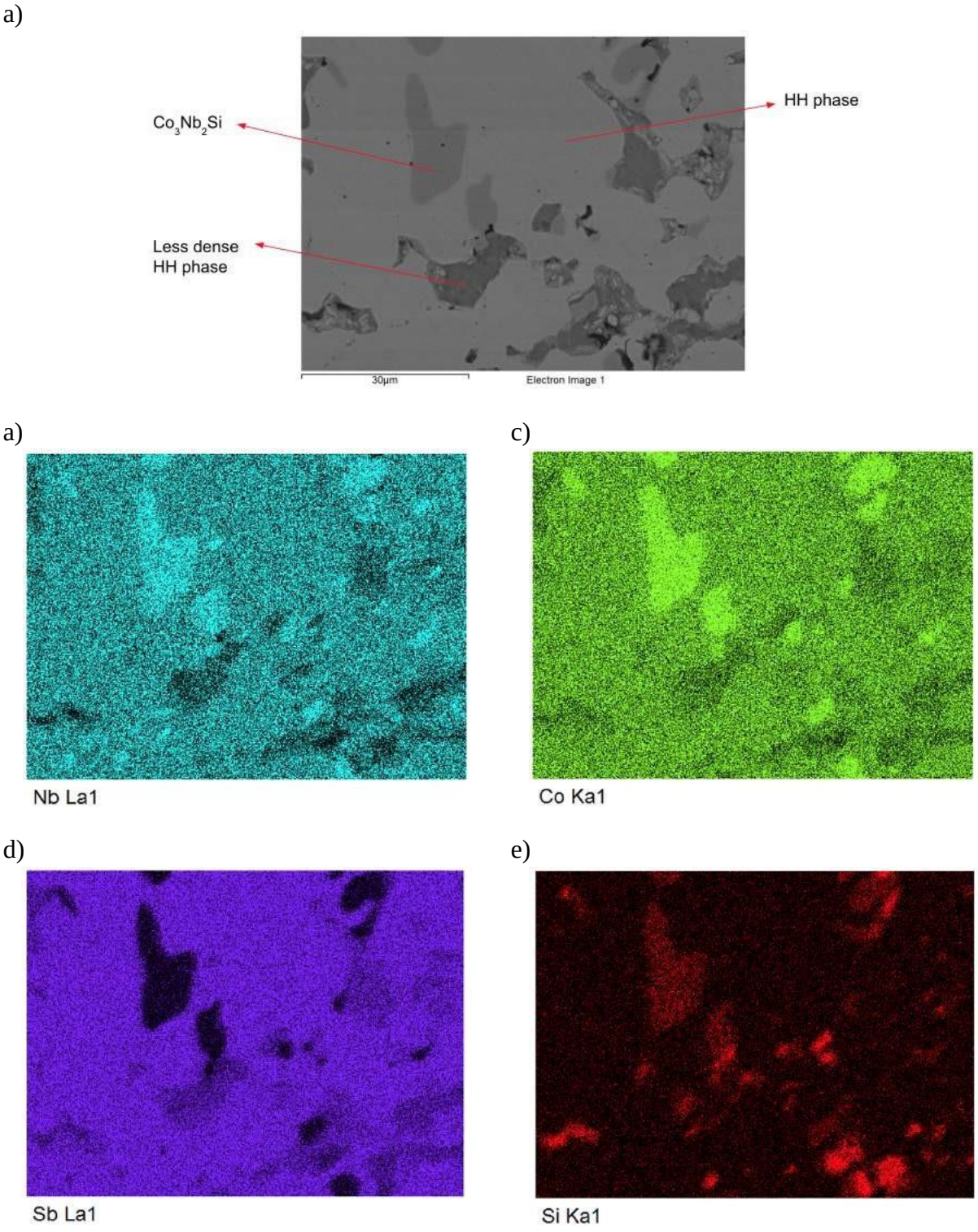

Fig 3.6: Chemical mapping of 2.5% Si doped sample at the Sb site of $Nb_{0.8}CoSb$

Later, the samples were hand-grinded again and hot-pressed. During the first attempt at hot pressing, the temperature and pyrometer settings were not optimized, and as a result, the 1% and 5% doped samples got melted away in the process. Ultimately, the 2.5% doped sample was successfully hot-pressed at a temperature of 1050^{o}C.

3.3.3 XRD of Hot-pressed sample

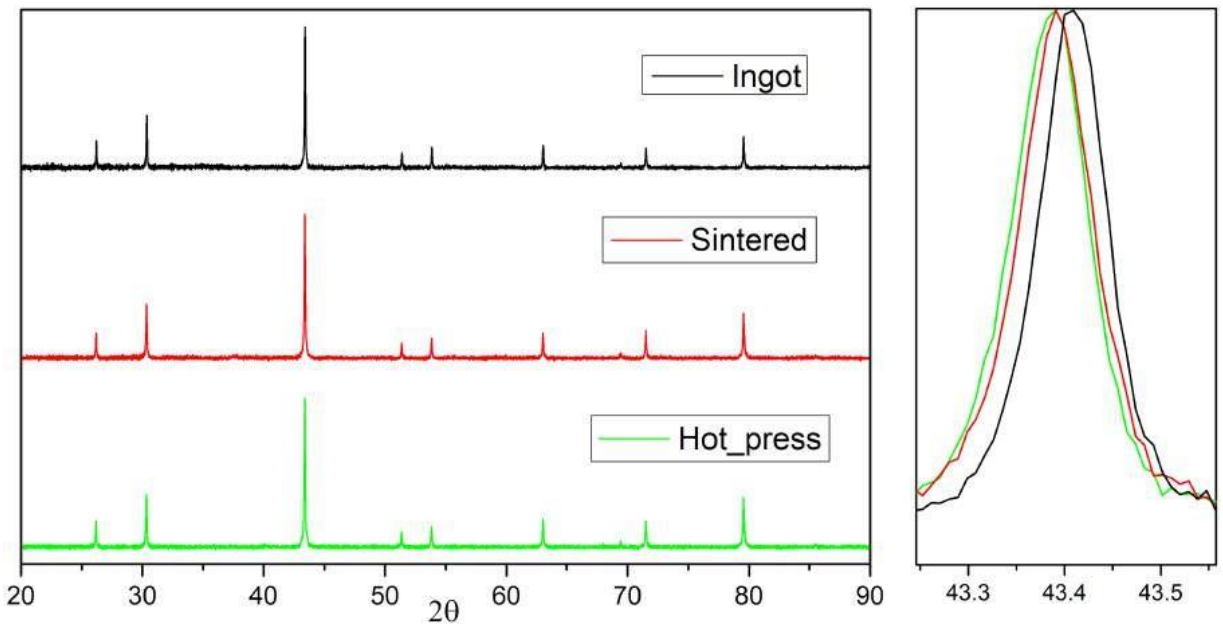

Fig 3.7: XRD and Peak Shift of 2.5% Si doped sample after Arcmelting, Sintering and Hot-press.

Even though the XRD analysis of the hot-pressed sample did not show any sign of the Co_3Nb_2Si phase, the FESEM images of the hot-pressed sample were similar to those of the sintered sample. It appears that the microstructure did not change upon hot-pressing, and we were able to obtain a dense cuboidal pellet.

3.3.4 Transport properties

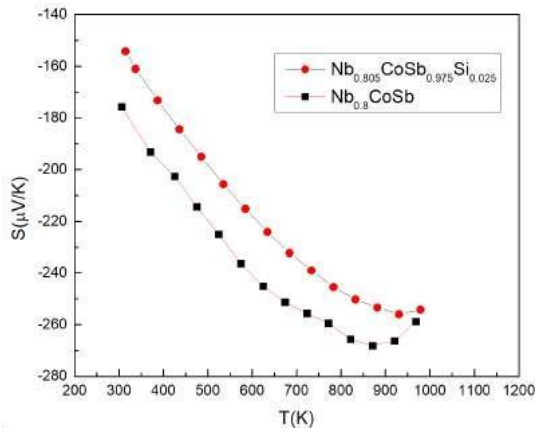

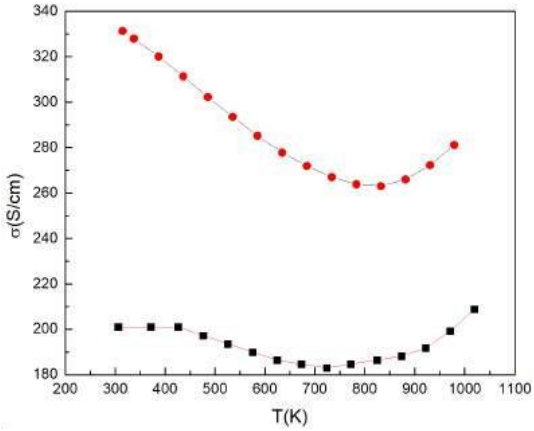

a) Seebeck Coefficient b) Electrical conductivity

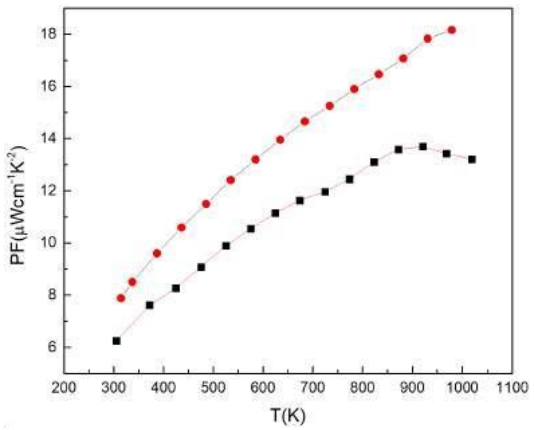

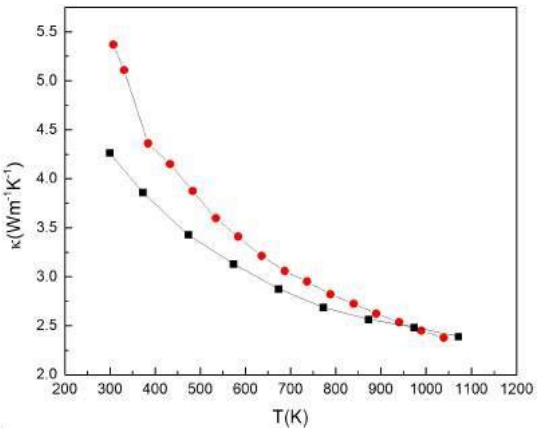

c) Power factor d) Thermal conductivity

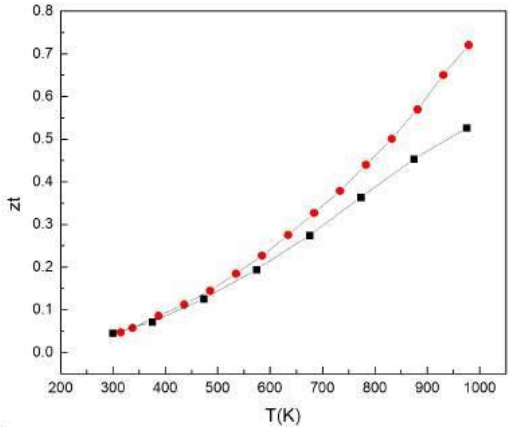

e) Figure of Merit(zt)

Fig 3.8: Thermoelectric properties 2.5% Si-sample and of $Nb_{0.8}CoSb$, which is taken from Xia et al[20]

The data for $Nb_{0.8}CoSb$ was regenerated from Xia et al using a web plot digitizer for comparison. The sample stoichiometry is $Nb_{0.805}CoSb_{0.975}Si_{0.025}$, which is nearly the same as $Nb_{0.8}CoSb$. On 2.5% Si-doped sample $Nb_{0.805}CoSb_{0.975}Si_{0.025}$ has a decreased Seebeck coefficient compared to $Nb_{0.8}CoSb$, and the electrical conductivity has increased. This could be due to the increase in carrier concentration as the matrix takes in more Nb. The bipolar temperature has slightly shifted to the right, indicating the rise in the Fermi level as carrier concentration increased. Consequently, the power factor has increased. The reason why the bipolar temperature is clear in electrical conductivity and not clear in Seebeck could be because of the less effective mass of minority carriers. Further analysis is needed to confirm this.

The thermal conductivity is similar at higher temperatures in both cases. However, at low temperatures, the difference in thermal conductivity could be due to the difference in electrical conductivity as it is significantly higher in the Si-doped sample. This data supports the hypothesis that the matrix takes in more Nb upon hole substitution at the Sb site. However, further investigation is needed with multiple dopings and reproducibility to prove this hypothesis.

3.4 Resonant Doping

I came across a paper on Resonant doping by Mitra et al, in which they achieved resonant doping in p-type $Hf_{0.3}Zr_{0.7}CoSn_{0.3}Sb_{0.7}$ by doping 1% Al at the Sb site[23], which enhanced the Seebeck coefficient without deteriorating the electrical conductivity. There was another report in which resonant doping was achieved in n-type $Hf_{0.75}Zr_{0.25}NiSn$ by doping 1% V at the Hf site which enhanced the thermoelectric properties[24]. In order to understand how the resonant dopant is chosen, we need to look at the band structures and electronegativity values.

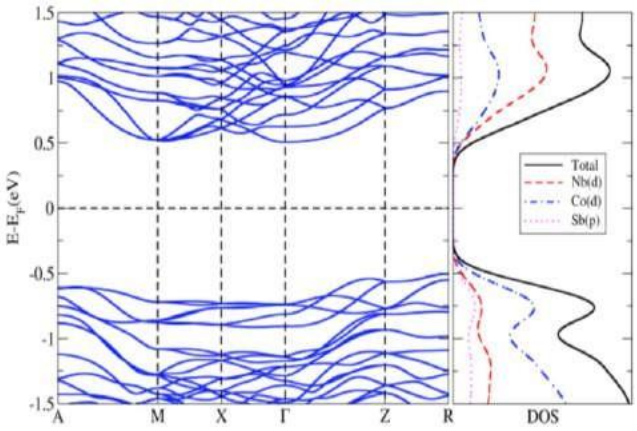

Fig 3.9: Band Structure of $Nb_{0.8}CoSb$ with DOS extracted from [21]

In the DOS band structure, Nb electronic states contribute more in the conduction band, Co electronic states contribute more at the top of the valence band, and Sb electronic states contribute more at the bottom of the valence band. The electronic state contribution is highly dependent on the element's electronegativity.

For resonant doping to occur, the dopant element should contribute electronic states at the Fermi level. In an n-type material (XYZ), the X site should be chosen for resonant doping, and the electronegativity of the dopant atom should exceed that of the X atom. In a p-type material, either the Y or Z site should be chosen for resonant doping, and the dopant's electronegativity should be less than that of Y or Z. This logic holds true for both $Hf_{0.3}Zr_{0.7}CoSn_{0.3}Sb_{0.7}$ and $Hf_{0.75}Zr_{0.25}NiSn$, where resonant doping was achieved through the appropriate choice of doping site and dopant electronegativity.

NbCoSb is an n-type material. To perform resonant doping, we should select the Nb site, and the electronegativity of the dopant should exceed that of Nb. The available elements are Mo and W. If we dope with Mo or W, the system would deviate further from 18 VEC, but we can design the stoichiometry in such a way that 18 VEC is maintained. I synthesized two samples, one with 1% Mo, and another with 1% W doping by arc melting. For this, Nb and Co were

melted first, and later Sb and Mo or W were added. The samples were then ground for 1 hour and hot-pressed at 1050°C.

3.4.1 XRD

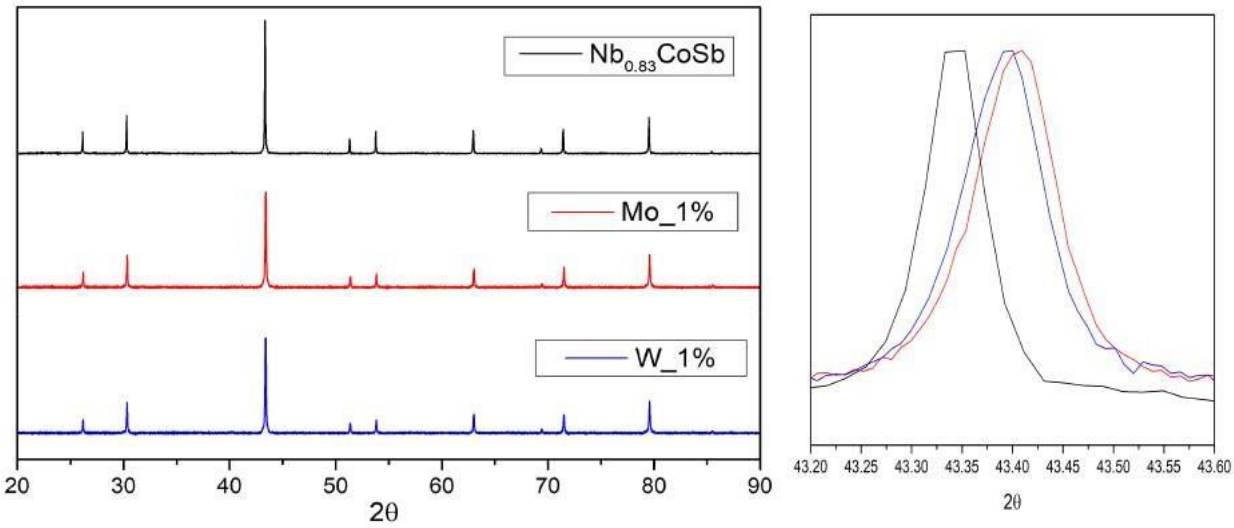

Fig 3.10: XRD and Peak shift of 1% doping of Mo and W at the Nb site of $Nb_{0.8}CoSb$

The XRD looks pure also the peaks shifted right indicating that the lattice parameters have decreased. Since $2dsin\theta = n\lambda$, if θ increases then d decreases for the same value of n. This result is expected if doping has occurred. The Shannon ionic radii of Nb, W, and Mo at coordination number 6 are 0.64 Å, 0.6 Å, and 0.59 Å, respectively. However, as we have observed in the case of Si doping, there may be impurities that are below the detectable range of XRD. Therefore, it is necessary to perform FESEM analysis to further examine the sample's purity.

3.4.2 FESEM

The chemical mapping of the tungsten-doped samples reveals the presence of an impurity phase of NbCo and a small region where elemental tungsten has segregated out. The reason for the presence of NbCo is likely due to the synthesis protocol, where Nb and Co were melted first before adding the other elements. It is possible that the NbCo did not completely melt as it was added as an ingot. Tungsten was not fully incorporated into the sample due to its high melting point, which is even higher than that of Nb.

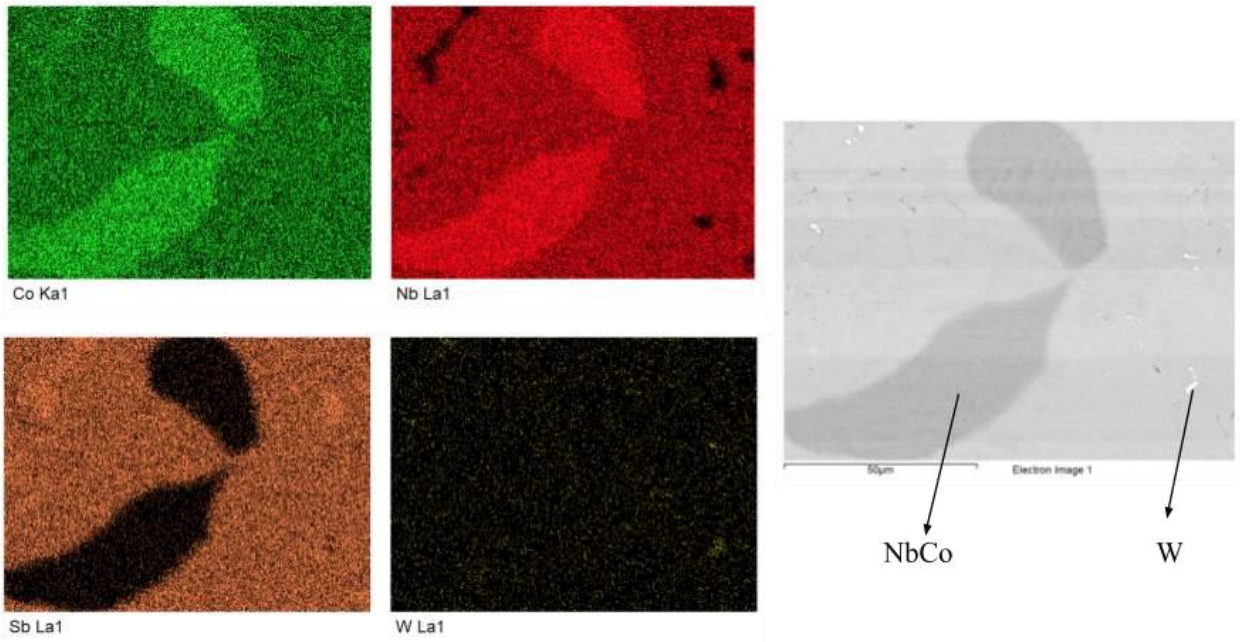

Fig 3.11: Chemical mapping of the 1% W doped sample

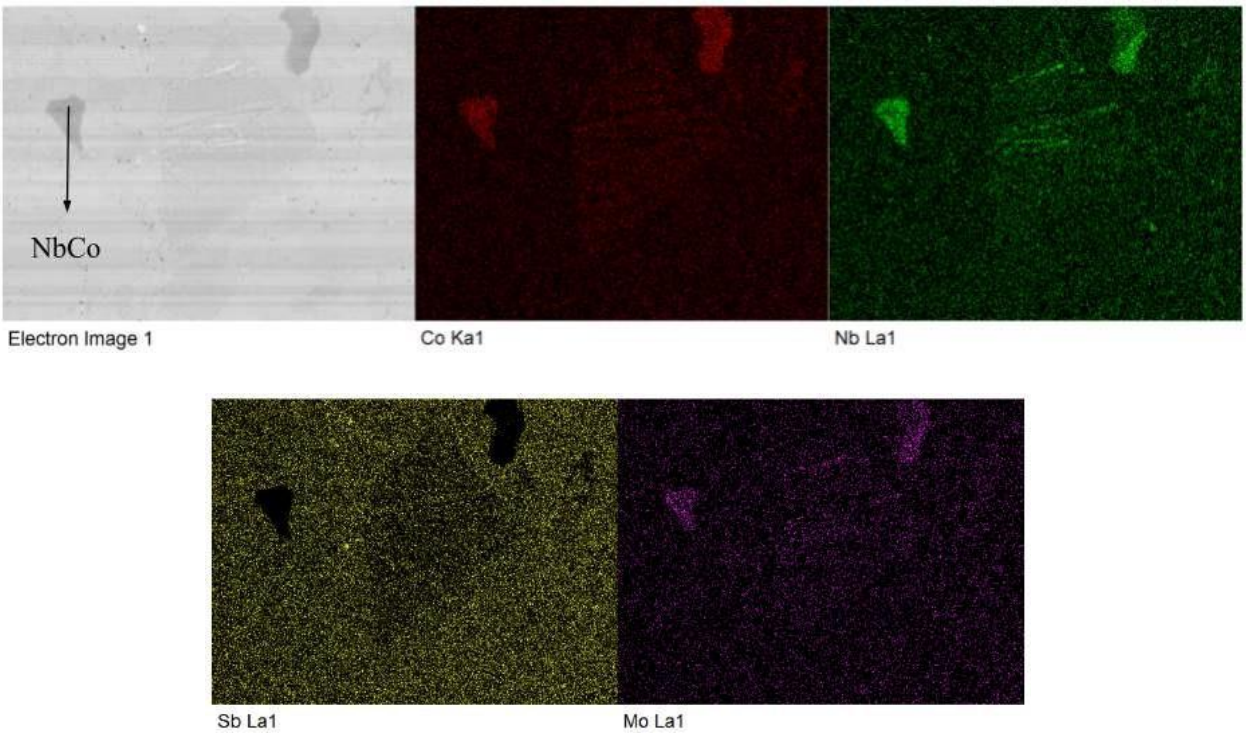

Fig 3.12: Chemical mapping of Mo_1% sample

In the Mo-doped sample, the NbCo phase is present due to the same synthesis method used as for the W-doped sample. Furthermore, an additional phase is observed in the figure, where the percentages of Nb and Co are slightly higher than Sb, while Mo is almost uniform. It is presumed to be a mixture of the main matrix with NbCo, but its identification is not yet fully confirmed.

3.4.3 Transport properties

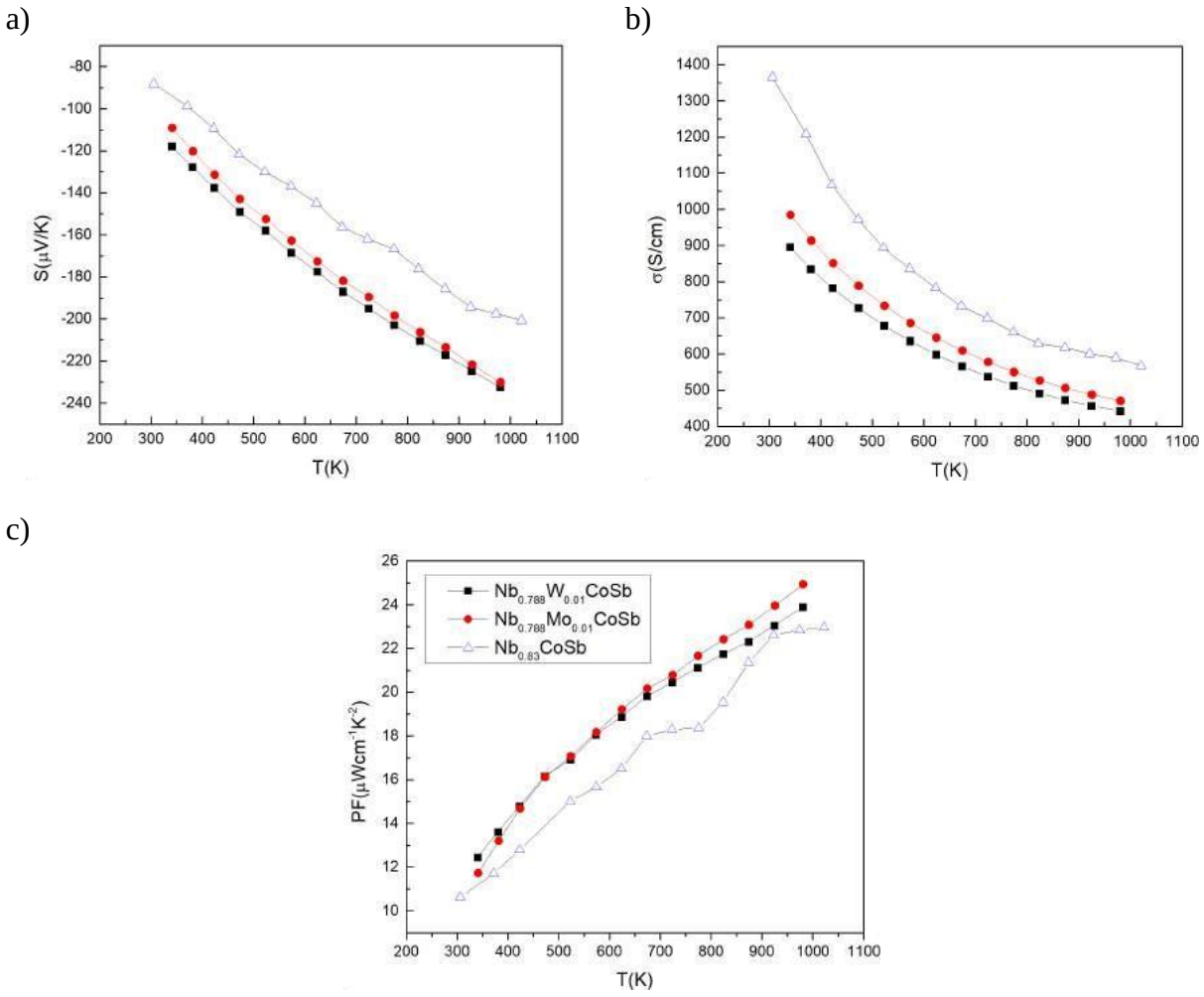

Fig 3.13: a) Seebeck coefficients b) electrical conductivity and c) power factors of 1% doping of Mo and W at the Nb site of $Nb_{0.8}CoSb$ and of $Nb_{0.83}CoSb$, which is taken from Xia et al[20] for comparison.

The transport properties of these samples are similar to those of $Nb_{0.8+x}CoSb$ with x ranging from 0.1-0.3, indicating that Mo and W are not creating resonant states but rather doping electrons into the matrix, similar to p and n-type doping in semiconductors. However, further samples with

different dopings of each element are necessary to support this argument and verify the expected properties.

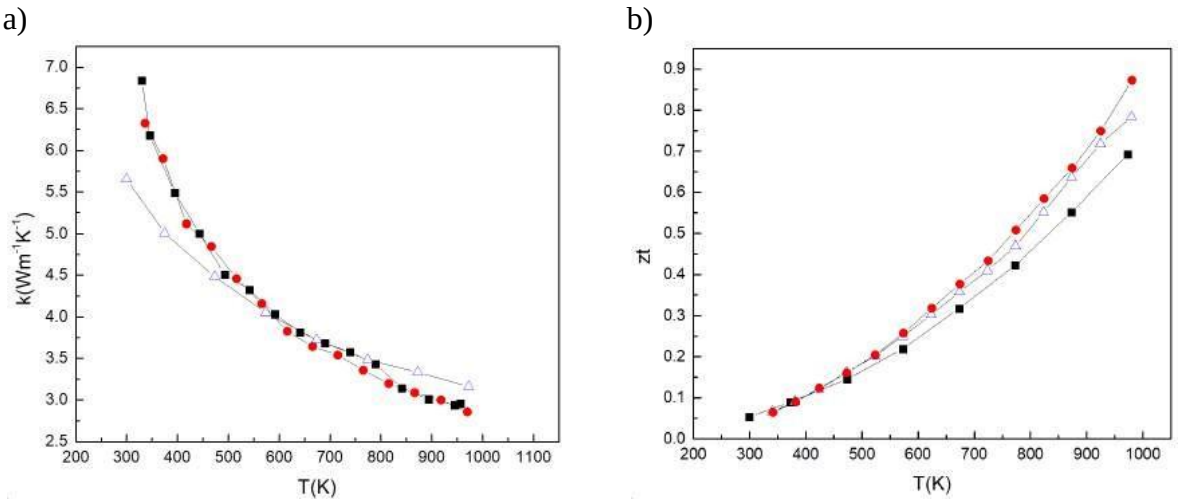

Fig 3.14: LFA and zT of 1% doping of Mo and W at the Nb site of $Nb_{0.8}CoSb$ and of $Nb_{0.83}CoSb$, which is extracted from Xia et al[20].

The zt value of $Nb_{0.83}CoSb$ was obtained from Xia et al. for comparison with the synthesized samples. The thermal conductivity of both the synthesized samples and the parent samples, $Nb_{0.8}CoSb$ and $Nb_{0.83}CoSb$, is similar due to maintaining vacancies and doping only 1% of the dopant, which is not strong enough to change the scattering mechanism. However, the thermal conductivity of the synthesized samples is greater than that of the parent samples, which is unusual. Upon studying the microstructure of both samples using FESEM, it was observed that the synthesized samples almost melted during the hot-pressing process, resulting in less grain boundary scattering.

3.5 Mo doping

I synthesized three samples with Mo dopings of 0.5%, 1%, and 1.5%, designed to maintain 18VEC stoichiometry. The chemical formulas of the samples are listed in the table. To avoid the presence of the impurity phase intermediate NbCo, which remains when Nb and Co are melted first, I melted all the elements at once. Instead of using Nb bars, I utilized small Nb pieces that were cut from an Nb rod, as depicted in Figure 2.1, for the melting process. Due to the reduced size of the Nb pieces, it is highly improbable that any Nb would remain unmelted.

The 0.5% and 1% samples were synthesized first, and during the grinding process, it was discovered that a small amount of Nb had not melted. The weight of the Nb pieces was on the order of milligrams, so the change in the stoichiometry of Nb would be small. Therefore, these pieces were removed before the samples were hot-pressed. For the 1.5% sample, even smaller Nb pieces were used and melted completely during the synthesis process. After grinding, this sample was also hot-pressed. All samples were hot-pressed at 1010°C.

3.5.1 XRD

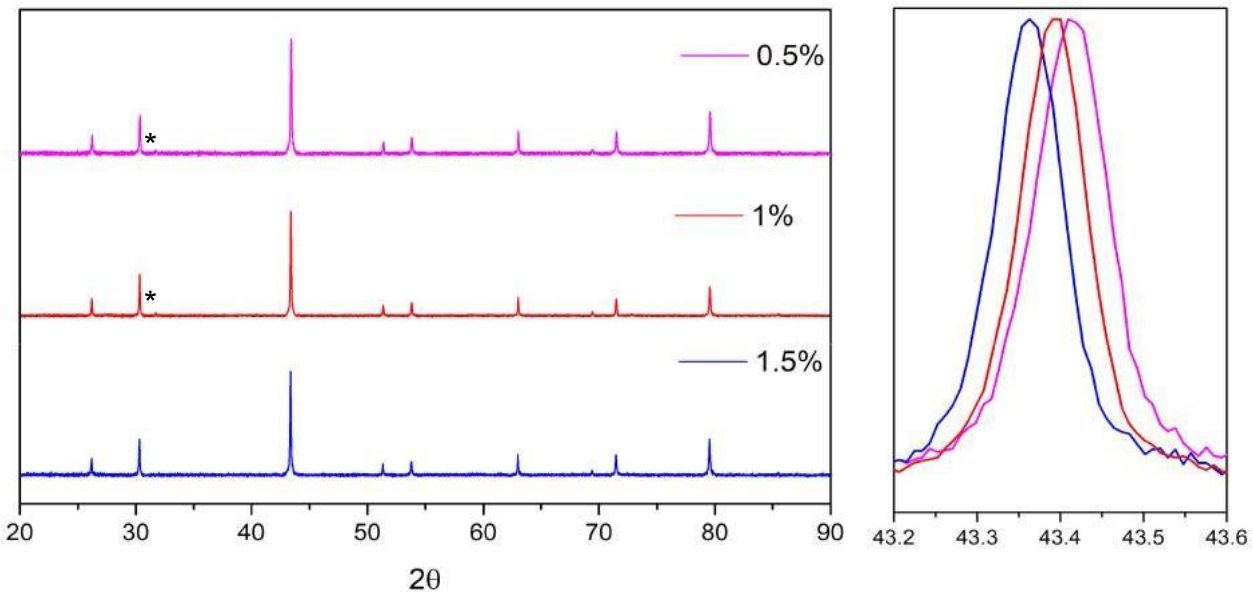

Fig 3.15: XRD and Peak Shift of the hot-Pressed 0.5%, 1% and 1.5% Mo doping at the Nb site of $Nb_{0.8}CoSb$

Sr No	Sample	Lattice parameter(A^o)
1	$Nb_{0.794}Mo_{0.005}CoSb$	5.8927
2	$Nb_{0.788}Mo_{0.01}CoSb$	5.8946
3	$Nb_{0.782}Mo_{0.015}CoSb$	5.8976

Table 3.4: Chemical formulae and the lattice parameters of 0.5%, 1% and 1.5% Mo doping at the Nb site of $Nb_{0.8}CoSb$

The XRD analysis shows that the main phase in all samples is the HH phase. However, the 0.5% and 1% doped samples have small amounts of CoSb phase due to some unmelting of Nb, whereas the 1.5% doped sample has no remaining Nb, and therefore no CoSb phase is present.

3.5.2 FESEM

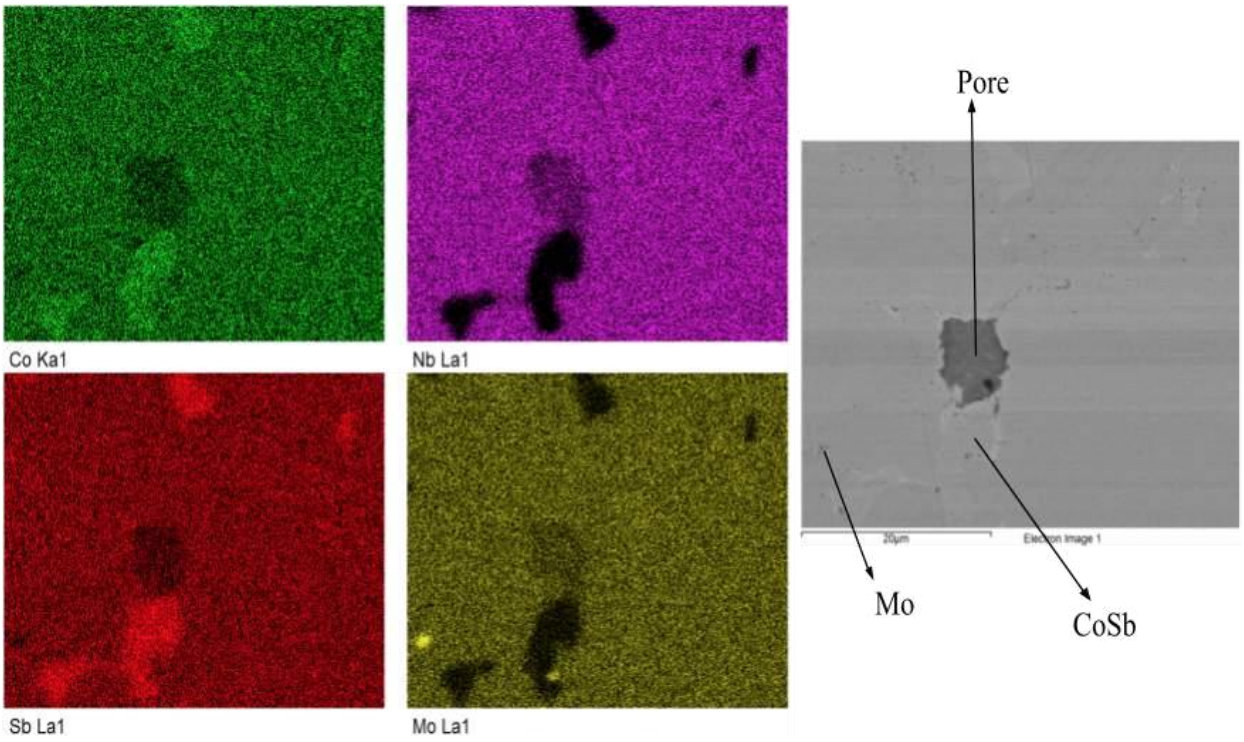

Fig 3.16:Chemical mapping of 1% Mo-doped hot-pressed sample

The chemical mapping of the 1% doped sample shows an impurity of CoSb and a small amount of Mo that segregated out. The image also has a phase which I believe to be a pore. This may be due to the low atomic percentages of all the elements and its dark appearance indicating fewer electrons and X-rays emanating from it. The following image shows a larger scale view in ASB and Inlens mode.

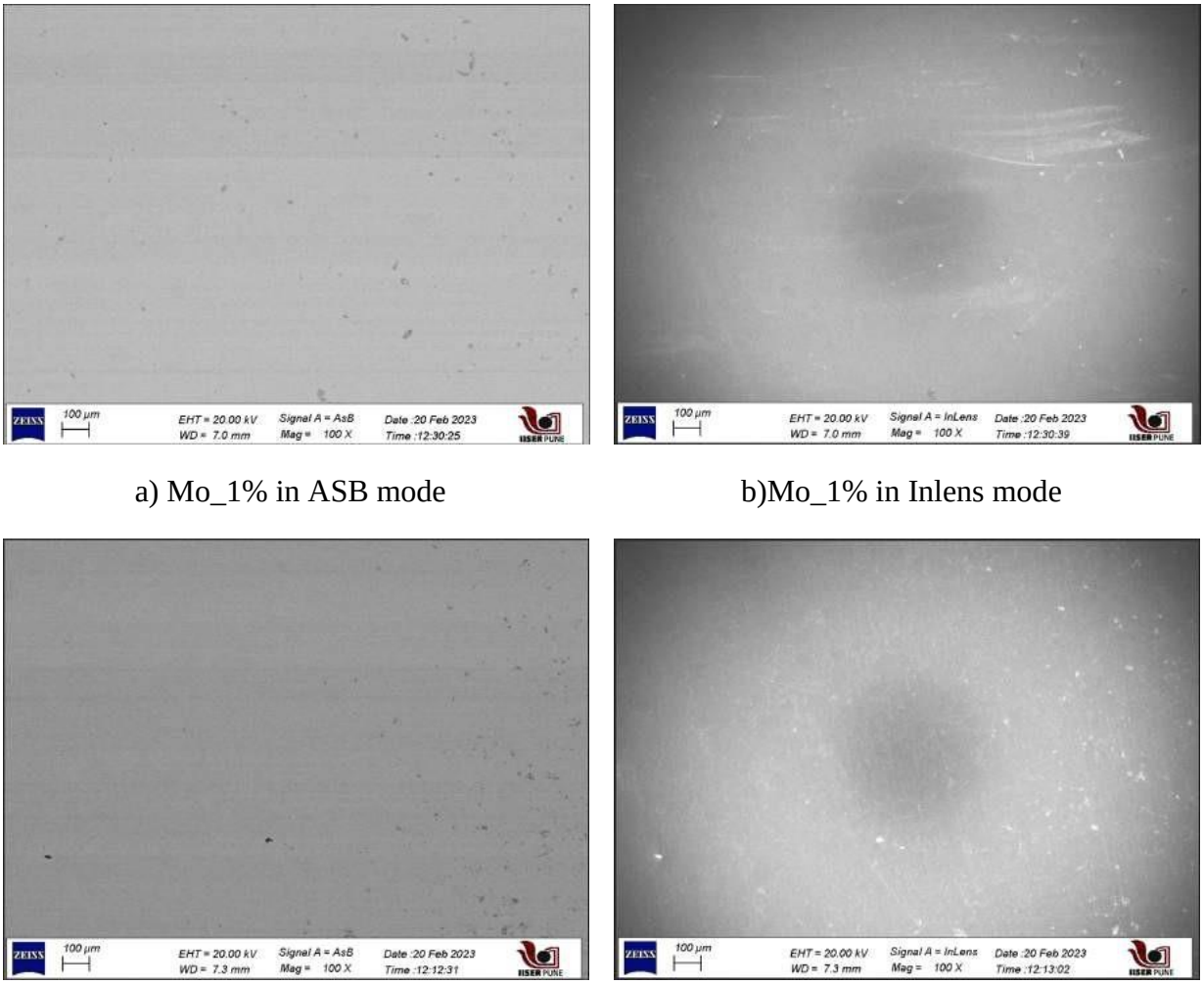

a) Mo_1% in ASB mode b)Mo_1% in Inlens mode

c) Mo_0.5% in ASB mode d) Mo_0.5% in Inlens mode

Fig 3.17: FESEM images modes of 0.5% and 1% Mo doped samples in ASB and Inlens

In both the 0.5% and 1% doped samples, the black spots observed in ASB mode appear in exactly the same positions where white spots are observed in Inlens mode. Since the Inlens mode provides information about morphology, the dark spots in the samples are likely due to the morphology, mostly pores. It is possible that these could be removed with ultrafine polishing.

3.5.2 Transport Properties

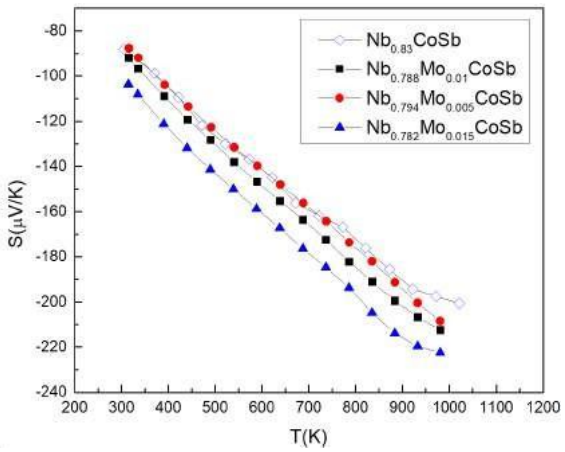

a) Seebeck Coefficient

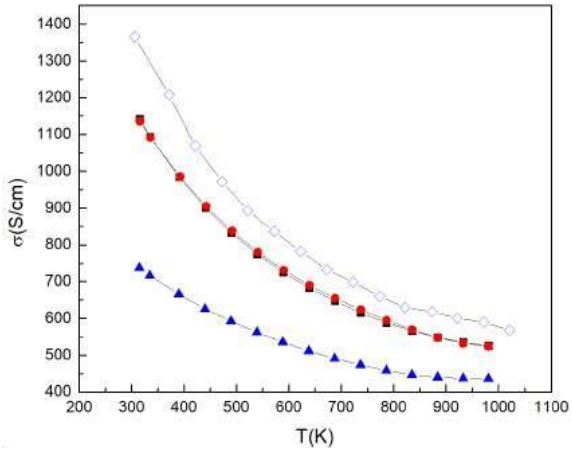

b) Electrical conductivity

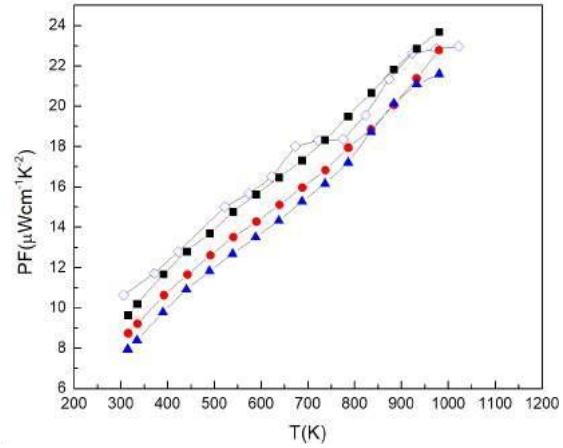

d) Power factor

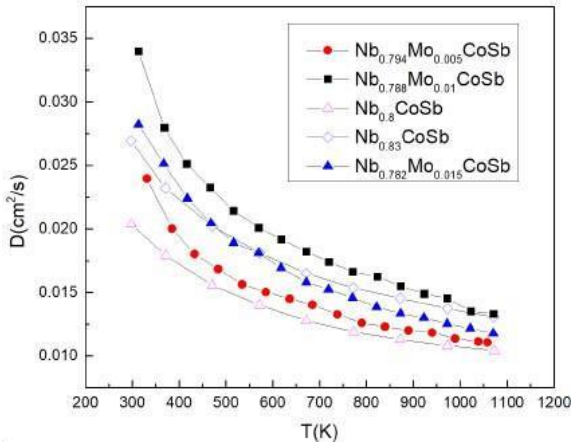

d) Thermal diffusivity

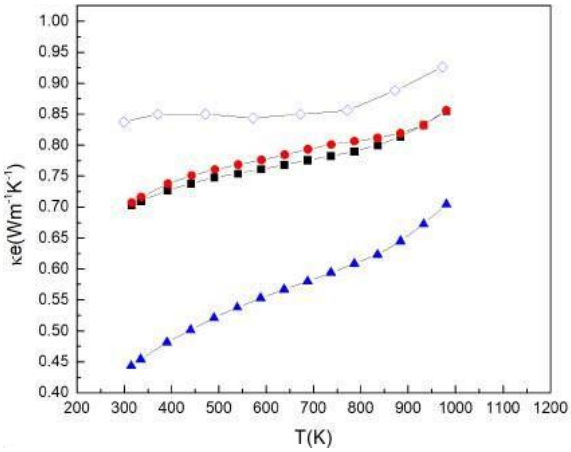

e) Electronic thermal conductivity

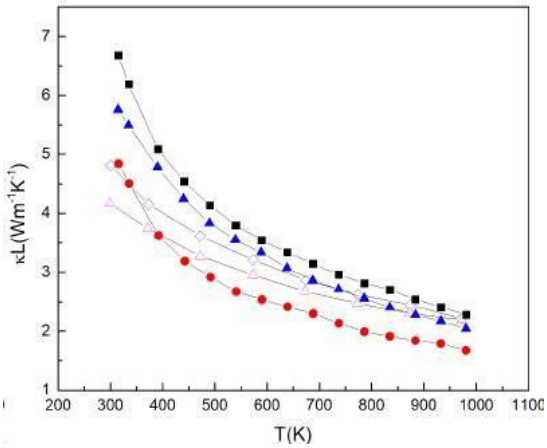

f) Lattice thermal conductivity

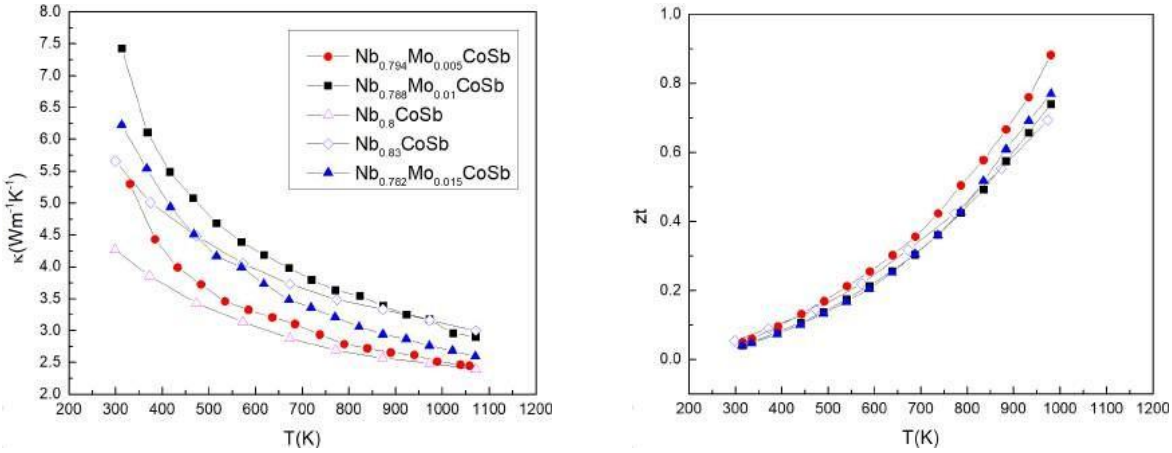

g) Thermal conductivity h) Figure of Merit (zt)

Fig 3.18: Transport properties of 0.5%, 1%, 1.5% Mo doping at the Nb site in $Nb_{0.8}CoSb$ and of $Nb_{0.83}CoSb$, $Nb_{0.8}CoSb$ extracted from Xia et al[20]

The data for $Nb_{0.8}CoSb$ and $Nb_{0.83}CoSb$ has been re-generated from Xia et al using web plot digitizer for comparison. Based on the results from the previous chapter, it was assumed that Mo was doping carriers into the matrix. However, this result does not prove that hypothesis. The electrical concentration does not increase with increasing Mo doping, and the Seebeck coefficient does not decrease in magnitude. Additionally, the thermal conductivity does not follow a particular order and there is a sudden decrease in the electrical conductivity of the 1.5% doped sample. Moreover, the Mo 1% sample prepared earlier behaves differently from the current 1% Mo sample, which could be attributed to the presence of the NbCo phase in the previous sample, but this is yet to be proven. Further analysis, such as Hall measurements and higher doping levels with reproducibility, are needed to understand the physics of Mo doping.

One thing is clear that it has enhanced the zT especially in the 0.5% doped sample because of the reduction in thermal conductivity, and the slope of zT indicates that at higher temperatures the enhancement would be even greater. Hence it is worth investigating it further.

Chapter-4

Conclusion

In three-fourths of my thesis, I investigated the substitution of the Sb site. Among the dopants, Al, Si, In, Ga, Sn, and Ge, only Al, Si, and Sn resulted in pure samples. Since Sn doping has already been studied, I explored Si and Al dopants. However, attempts to achieve an Nb stoichiometry of 0.9 through higher dopings of Al and Si resulted in the formation of impurity phases, making it impossible to synthesize a sample with an Nb stoichiometry of 0.9 through z-site doping.

Then, lower doping Si samples were synthesized, but unfortunately, the 1% and 5% samples melted away during the hot press optimization process. The measurements on these samples support the hypothesis that hole doping increases the amount of Nb in the matrix, but further investigation is needed. However, the enhancement in transport properties is not enough to exceed the performance of Nb0.83CoSb, and the lack of clarity in the Si samples does not provide strong motivation to pursue it further. Additionally, the lower doping of Al has not been explored yet.

In the next quarter of my MS, I attempted resonant doping in Nb0.8CoSb using Mo and W. I prepared 1% doping of each, but resonant doping did not occur. However, the results were intriguing, as it appeared that Mo might be doping carriers into the matrix. However, the lower doping study of Mo did not support this hypothesis, and further analysis is needed to understand the underlying physics. Additionally, W doping has yet to be explored.

Bibliography

[1] Flowcharts(https://flowcharts.llnl.gov/)

[2] Mahan G D 2016 Introduction to thermoelectrics *APL Mater.* **4** 104806

[3] Neeli G, Behara D K and Kumar M K 2013 State of the Art Review on Thermoelectric Materials **5**

[4] Chaturvedi K M 2014 "Synthesis and Investigation of Thermo-Electric properties of Skutterudites CoSb3/Graphene particles nanocomposite"

[5] Badgujar G S 2015 To Enhance the Heat Transfer Rate in Thermoelectric Cooler: A Review *Int. J. Innov. Eng. Technol.* **5**

[6] Goldsmid H J 2016 *Introduction to Thermoelectricity* vol 121 (Berlin, Heidelberg: Springer Berlin Heidelberg)

[7] Kurosaki K, Shi X and Takagiwa Y 2020 *Thermoelectric materials: principles and concepts for enhanced properties* (Berlin ; Boston: De Gruyter)

[8] Kim H-S, Gibbs Z M, Tang Y, Wang H and Snyder G J 2015 Characterization of Lorenz number with Seebeck coefficient measurement *APL Mater.* **3** 041506

[9] Brown, David Ross 2014 *Enhanced Thermoelectric Performance at the Superionic Phase Transitions of Mixed Ion-Electron Conducting Materials* (California Institute of Technology)

[10] Anon 2022 What are P-type & N-type Silicon Semiconductors? | Stanford Advanced Materials *Glob. Supplier Sputtering Targets Evaporation Mater. Stanf. Adv. Mater.*

[11] Liu W, Tan X, Yin K, Liu H, Tang X, Shi J, Zhang Q and Uher C 2012 Convergence of Conduction Bands as a Means of Enhancing Thermoelectric Performance of n -Type Mg 2 Si 1 − x Sn x Solid Solutions *Phys. Rev. Lett.* **108** 166601

[12] Zebarjadi M, Joshi G, Zhu G, Yu B, Minnich A, Lan Y, Wang X, Dresselhaus M, Ren Z and Chen G 2011 Power Factor Enhancement by Modulation Doping in Bulk Nanocomposites *Nano Lett.* **11** 2225–30

[13] Anon Electron mobilities in modulation-doped semiconductor heterojunction superlattices: Applied Physics Letters: Vol 33, No 7

[14] Martin J, Wang L, Chen L and Nolas G S 2009 Enhanced Seebeck coefficient through energy-barrier scattering in PbTe nanocomposites *Phys. Rev. B* **79** 115311

[15] Yan X, Joshi G, Liu W, Lan Y, Wang H, Lee S, Simonson J W, Poon S J, Tritt T M, Chen G and Ren Z F 2011 Enhanced Thermoelectric Figure of Merit of p-Type Half-Heuslers

Nano Lett. **11** 556–60

[16] Wang R-F, Li S, Xue W-H, Chen C, Wang Y-M, Liu X-J and Zhang Q 2021 Enhanced thermoelectric performance of n-type TiCoSb half-Heusler by Ta doping and Hf alloying *Rare Met.* **40** 40–7

[17] Asheghi M, Kurabayashi K, Kasnavi R and Goodson K 2002 Thermal conduction in doped single-crystal silicon films *J. Appl. Phys.* **91** 5079–88

[18] Xie W, Weidenkaff A, Tang X, Zhang Q, Poon S and Tritt T M 2012 Recent Advances in Nanostructured Thermoelectric Half-Heusler Compounds *Nanomaterials* **2** 379

[19] Graf T, Felser C and Parkin S S P 2011 Simple rules for the understanding of Heusler compounds *Prog. Solid State Chem.* **39** 1–50

[20] Xia K, Liu Y, Anand S, Snyder G J, Xin J, Yu J, Zhao X and Zhu T 2018 Enhanced Thermoelectric Performance in 18-Electron Nb $_{0.8}$ CoSb Half-Heusler Compound with Intrinsic Nb Vacancies *Adv. Funct. Mater.* **28** 1705845

[21] Saurabh K 2022 *Study of half-Heusler and related structures as high-temperature thermoelectrics* Thesis (Dept. of Physics)

[22] Anon Scanning Electron Microscope - Radiological and Environmental Management - PurdueUniversity(https://www.purdue.edu/ehps/rem/laboratory/equipment%20safety/Research%20Equipment/sem.html)

[23] Mitra M, Benton A, Akhanda M S, Qi J, Zebarjadi M, Singh D J and Poon S J 2022 Conventional Half-Heusler alloys advance state-of-the-art thermoelectric properties *Mater. Today Phys.* **28** 100900

[24] Simonson J W, Wu D, Xie W J, Tritt T M and Poon S J 2011 Introduction of resonant states and enhancement of thermoelectric properties in half-Heusler alloys *Phys. Rev. B* **83** 235211